Check for updates

Small

NANO · MICRO small
www.small-journal.com

RESEARCH ARTICLE OPEN ACCESS

Hierarchically Engineered Nanocellulose-Halloysite Composite Foams for Integrated Thermal Insulation and Intrinsic Fire Resistance

Tamilselvan Mohan[1,2] | Doris Bračič[3] | Chandran Nagaraj[2,4] | Thomas Harter[5] | Resul Fener[6] | Anne Dennstedt[7] | Barbara Milow[6,8] | Kathirvel Ganesan[6] | Ulrich Hirn[5] | Rupert Kargl[1] | Karin Stana Kleinscheck[1]

[1]Institute of Chemistry and Technology of Biobased System (IBioSys), Graz University of Technology, Graz, Austria | [2]BioMedTech, Graz, Austria | [3]Faculty of Mechanical Engineering, University Laboratory for Characterization and Processing of Polymers, of Maribor, Maribor, Slovenia | [4]Division of Respiratory Medicine, Lung Research Cluster, Department of Internal Medicine, Medical University of Graz, Graz, Austria | [5]Graz University of Technology, Institute of Bioproducts and Paper Technology, Graz, Austria | [6]German Aerospace Center (DLR), Institute for Frontier Materials on Earth and in Space, Department of Aerogels and Highly Porous Materials, Cologne, Germany | [7]German Aerospace Center (DLR), Institute for Frontier Materials on Earth and in Space, Department of Digitally Integrated Microstructure and Mechanics, Cologne, Germany | [8]University of Cologne (UoC), Department of Chemistry, Institute of Inorganic and Materials Chemistry, Nanostructured Cellular Materials, Cologne, Germany

Correspondence: Tamilselvan Mohan (tamilselvan.mohan@tugraz.at) | Karin Stana Kleinscheck (karin.stanakleinschek@tugraz.at)

Received: 2 April 2026 | **Revised:** 15 September 2026 | **Accepted:** 17 September 2026

Keywords: fire-resistance | foam | halloysite | mechanical properties | nanocomposite | nanofibrillated cellulose | thermal insulation

ABSTRACT

Achieving the simultaneous integration of thermal insulation, mechanical robustness, hydrophobicity, and intrinsic flame retardancy in bio-based porous materials remains a major challenge. Here, we report a hierarchically engineered nanocomposite foam composed of nanofibrillated cellulose (NFC), alkyl ketene dimer (AKD), and halloysite nanotubes (HNT), designed via a multiscale structure–property approach. Incorporation of HNT (1–10 wt%) reinforces the fibrillar network and introduces a hierarchical macro–mesoporous architecture, while AKD imparts durable hydrophobicity with water contact angles of 133–154°. The foams exhibit low thermal conductivity (0.031–0.046 W m^{-1} K^{-1}), high compressive modulus (~1.1 MPa), and excellent deformability (~80% strain). The materials display outstanding flame retardancy, with combustion velocities reduced by over an order of magnitude (~6 to ~0.1 cm s^{-1}) and clear self-extinguishing behavior. Thermal analysis reveals enhanced stability and increased char yield (~45%), consistent with modified degradation pathways. Thermal cycling tests (10 cycles, 25°C–80°C) confirm structural stability with no pore collapse and negligible change in thermal conductivity (≤2.2%). This multifunctionality arises from the synergy between halloysite-induced barrier effects, hierarchical structural reinforcement, and controlled interfacial chemistry, providing a scalable route to sustainable, lightweight, and fire-safe insulation materials without toxic additives.

Tamilselvan Mohan and Rupert Kargl Members of the European Polysaccharide Network of Excellence (EPNOE).

This is an open access article under the terms of the Creative Commons Attribution License, which permits use, distribution and reproduction in any medium, provided the original work is properly cited.
© 2026 The Author(s). *Small* published by Wiley-VCH GmbH

1 | Introduction

The transition toward energy-efficient and carbon-neutral technologies demands the development of next-generation functional materials that combine low thermal conductivity, mechanical resilience, and intrinsic fire safety within sustainable frameworks. Conventional polymeric insulation materials, including expanded polystyrene (EPS), polyurethane (PU), and phenolic foams, offer excellent thermal performance (≈0.02–0.04 W m^{-1} K^{-1}) [1, 2], yet their dependence on fossil resources, limited recyclability, and high flammability present persistent environmental and safety challenges [3, 4]. In contrast, inorganic systems such as silica aerogels can achieve ultralow thermal conductivities (<0.02 W m^{-1} K^{-1}) [5, 6], but their brittleness, processing complexity, and high cost restrict practical implementation. These limitations highlight a critical need for lightweight, multifunctional, and sustainable materials that overcome the traditional trade-offs between insulation performance, structural integrity, and fire resistance [7, 8]. Bio-based porous materials derived from polysaccharides have emerged as promising alternatives due to their renewability, low density, and tunable hierarchical structures [7, 9, 10]. Among these, nanofibrillated cellulose (NFC) represents a uniquely versatile building block, combining nanoscale dimensions, high aspect ratio, and a percolating hydrogen-bonded network that enables mechanically robust yet highly porous architectures [11–13]. NFC-based aerogels and foams typically exhibit thermal conductivities in the range of 0.03–0.05 W m^{-1} K^{-1}, approaching those of commercial insulators while offering superior sustainability [5, 14]. However, their broader adoption is hindered by two intrinsic limitations: (i) high flammability, arising from rapid thermal depolymerization and volatile release, and (ii) strong hydrophilicity, which leads to moisture uptake, structural instability, and degradation of thermal insulation under humid conditions [15–17].

Efforts to address these challenges have largely relied on additive-based strategies that remain fundamentally constrained [5, 18]. Conventional halogen- or phosphorus-based flame retardants introduce toxicity and environmental persistence, while inorganic fillers such as nanoclays and metal hydroxides improve fire resistance but often compromise porosity, density, or thermal transport [19, 20]. Similarly, surface hydrophobization approaches frequently disrupt the delicate pore architecture required for efficient insulation [21, 22]. As a result, the simultaneous realization of flame retardancy, hydrophobicity, mechanical robustness, and low thermal conductivity within a fully bio-derived system remains an unresolved challenge, largely due to the lack of integrated design principles that couple chemistry, structure, and transport phenomena across multiple length scales [23, 24].

Here, we introduce a hierarchically engineered nanocomposite foam that integrates NFC, halloysite nanotubes (HNTs), and alkyl ketene dimer (AKD) to overcome these limitations through a synergistic multiscale design strategy. Halloysite, a naturally occurring aluminosilicate with a unique nanotubular morphology, serves as both a mechanical reinforcing phase and an intrinsic flame-retardant component, promoting char formation, suppressing heat release, and introducing tortuous pathways that impede heat and mass transport during combustion [25–27]. Halloysite nanotubes were selected in preference to other clay-based fillers such as montmorillonite or sepiolite because their tubular morphology and high aspect ratio enable strong mechanical interlocking with the NFC network [28, 29], while the aluminosilicate shell provides efficient barrier effects during combustion without excessively increasing the solid fraction. In contrast to plate-like clays, which often induce pronounced densification and loss of porosity at comparable loadings [5], halloysite allows us to preserve the hierarchical macro-mesoporous architecture that is essential for low thermal conductivity, while simultaneously enhancing mechanical robustness and flame retardancy. Concurrently, AKD provides hydrophobic modification of the cellulose network, enabling moisture resistance while preserving the hierarchical porous architecture essential for thermal insulation [21, 30]. Importantly, this work advances the current state of the art in several key ways. First, the incorporation of HNT enables effective flame retardancy and helps preserve the foam structure during combustion, without the need for toxic additives, resulting in near self-extinguishing behavior while maintaining low density. Second, the hydrophobic modification using AKD allows the material to retain low thermal conductivity, comparable to high-performance nanocellulose aerogels, even after introducing inorganic fillers. Third, by combining structural and thermal analyses, we show how the nanofoam structure and composition directly influence its overall performance, providing clear insights for designing multifunctional insulation materials.

2 | Results and Discussion

2.1 | Design and Fabrication of Multifunctional NFC-AKD-HNT Nanocomposite Foams

To address the demand for lightweight, multifunctional, and fire-safe insulation materials, nanocomposite foams based on NFC, AKD, and HNT were rationally designed and systematically investigated. The fabrication of such materials is critical, as their performance is governed by the interplay between composition and hierarchical porous architecture. In this system, NFC serves as the primary structural matrix due to its ability to form a percolating nanofibrillar network that enables the development of highly porous and mechanically resilient structures. HNTs were incorporated as multifunctional inorganic nanofillers to reinforce the fibrillar network and impart flame-retardant functionality. Concurrently, AKD was introduced to modify the surface chemistry and reducing wettability without compromising the structural integrity of the porous network. To assess the colloidal behavior of the HNT dispersions prior to foam fabrication, DLS analysis was performed. DLS analysis of the HNT dispersions revealed a systematic increase in hydrodynamic size and a broadening of the size distribution with increasing HNT concentration (see Figure S1). The 1 wt% (NAH1) dispersion showed the smallest and narrowest population, consistent with a more stable and better-dispersed suspension. In contrast, the 5 wt% (NAH5) and especially the 10 wt% (NAH10) dispersions exhibited larger apparent particle sizes and broader distributions, indicating stronger particle association and reduced colloidal stability at higher loading. Because DLS reflects hydrodynamic behavior in suspension rather than direct particle imaging, these results are best interpreted as evidence of increasing

16136829, 0, Downloaded from https://onlinelibrary.wiley.com/doi/10.1002/smll.75920 by Dtsch Zentrum F. Luft-U. Raum Fahrt In D. Helmholtz Gemein., Wiley Online Library on [27/09/2026]. See the Terms and Conditions (https://onlinelibrary.wiley.com/terms-and-conditions) on Wiley Online Library for rules of use; OA articles are governed by the applicable Creative Commons License

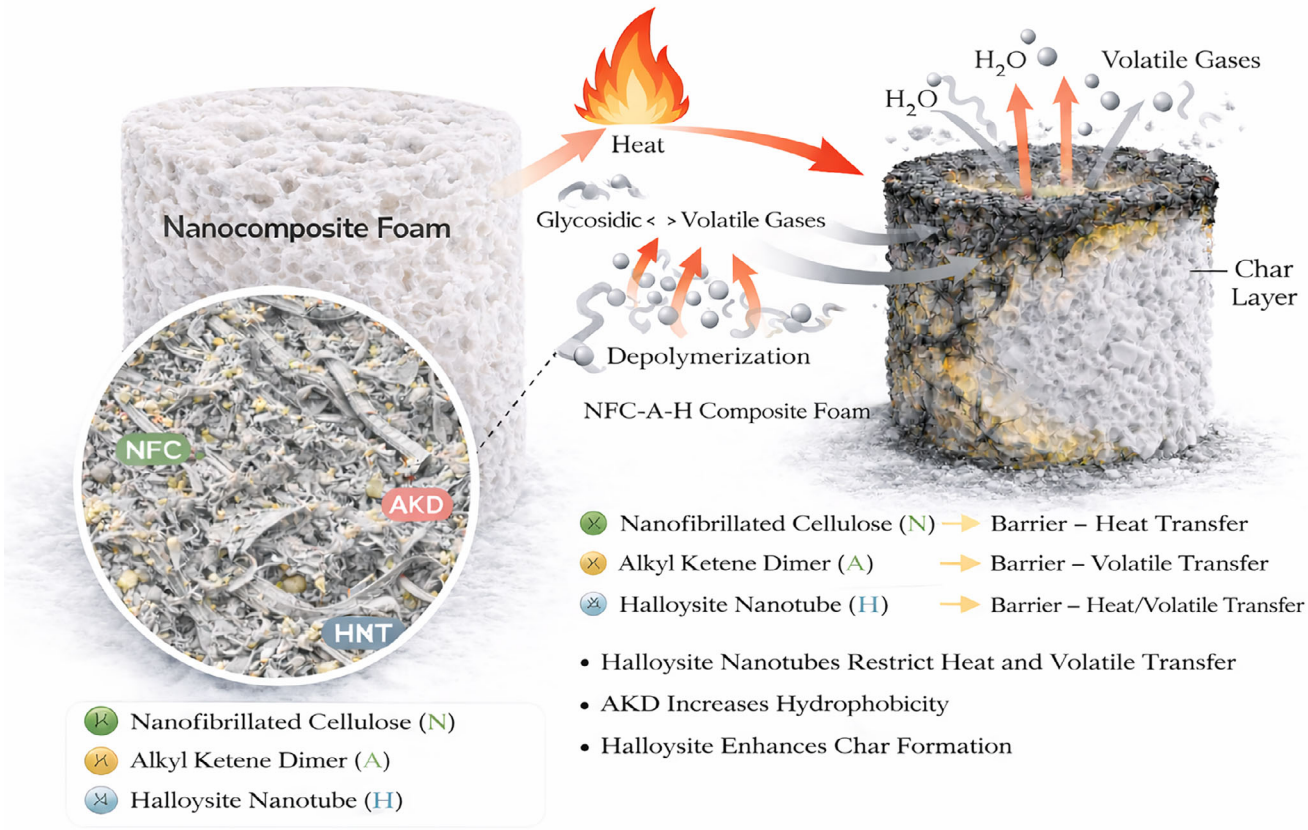


FIGURE 1 | Schematic illustration of the structure and flame-retardant mechanism of NFC–AKD–HNT nanocomposite foams.

nanotube clustering or loose agglomeration with increasing HNT content [31]. The nanocomposite foams were fabricated via a controlled dispersion and homogenization process, followed by casting and freeze-drying. This approach enables the formation of a 3D, interconnected porous architecture with uniform distribution of HNT within the NFC matrix (Figure 1). The resulting structure exhibits a well-defined hierarchical organization, where inorganic nanotubes are embedded within the pore walls, contributing to both structural reinforcement and functional performance. This fabrication strategy allows precise control over composition and microstructure, leading to nanocomposite foams with tunable properties. The following sections systematically elucidate how the engineered hierarchical architecture governs the thermal transport, mechanical behavior, and flame-retardant performance of the materials.

2.2 | Chemical and Structural Properties of Nanocellulose Composite Foam

The FTIR spectra and corresponding peak values of neat NFC and NFC–AKD–HNT composite foams are shown in Figure 2a and summarized in Table S1.The neat NFC (Figure 2a, i) exhibits characteristic cellulose peaks: the broad O—H stretching peak at ~3330 cm^{-1}, C—H stretching at ~2895 cm^{-1}, and the H—O—H bending of absorbed moisture around ~1640 cm^{-1}, glycosidic C-O at 1035 cm^{-1}, and ring vibrations between 1150–1300 cm^{-1} [32–34]. Upon incorporation of AKD and HNT, distinct spectral changes are observed. The appearance of new peaks at ~2917 and ~2850 cm^{-1} is attributed to the asymmetric and symmetric stretching vibrations of the long alkyl chains of AKD, indicating successful introduction of hydrophobic moieties [35]. A carbonyl peak at ~1720 cm^{-1} is also observed, which can be associated with the presence of AKD. This peak likely arises from β-keto ester structures formed through interaction between AKD and cellulose hydroxyl groups, although contributions from unreacted or hydrolyzed AKD cannot be excluded under the neutral conditions employed [35]. Such interactions are commonly reported as the primary mechanism for cellulose surface hydrophobization [36]. To distinguish covalent AKD–cellulose interactions from physical adsorption, FTIR spectra of neat AKD, NFC, and a physically mixed NFC/AKD control (air-dried without thermal treatment) were recorded (Figure S2) and compared with the spectra of the nanocomposite foams shown in Figure 2a. The neat AKD spectrum, besides other characteristic features, displays two carbonyl features: a β-lactone C═O stretch at ~1849 cm^{-1}, arising from the intact four-membered lactone ring of unreacted AKD, and a β-keto C═O stretch at ~1700 cm^{-1}. The physically mixed NFC/AKD control retains the β-lactone peak at ~1849 cm^{-1} with no carbonyl peak at ~1720 cm^{-1}, confirming that physical contact between AKD and cellulose alone does not generate β-keto ester carbonyl features. In contrast, the NFC–AKD–HNT foams (Figure 2a) show a marked reduction in the intensity of the β-lactone peak at ~1849 cm^{-1} and the concurrent emergence of a new peak at ~1720 cm^{-1}. The reduction of the β-lactone C═O, together with the appearance of the ~1720 cm^{-1} peak that is absent in the physical mixture, directly evidences partial ring-opening of the AKD lactone by nucleophilic attack from cellulose

16136829, 0, Downloaded from https://onlinelibrary.wiley.com/doi/10.1002/smll.75920 by Dtsch Zentrum F. Luft-U. Raum Fahrt In D. Helmholtz Gemein., Wiley Online Library on [27/09/2026]. See the Terms and Conditions (https://onlinelibrary.wiley.com/terms-and-conditions) on Wiley Online Library for rules of use; OA articles are governed by the applicable Creative Commons License

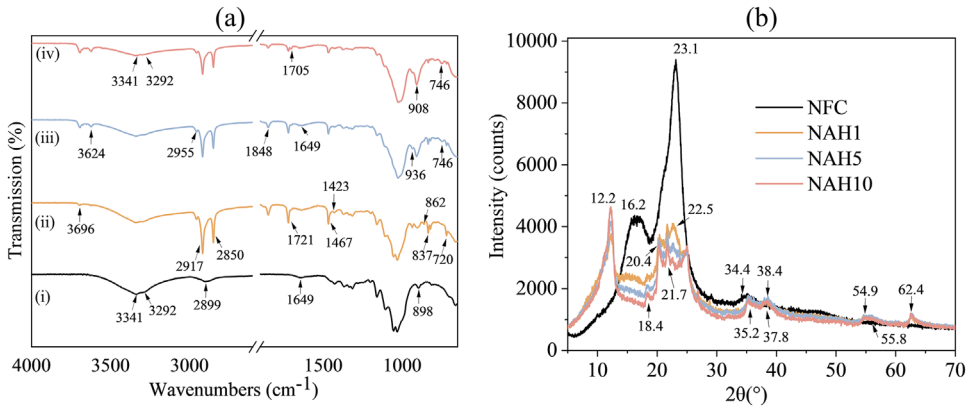


FIGURE 2 | FTIR spectra (a) and powder XRD patterns (b) of neat NFC and NAH1 – NAH10 nanocomposite foams.

hydroxyl groups. This confirms that the ~1720 cm^{-1} peak arises from covalently formed β-keto ester structures. The residual β-lactone signal in the foams is consistent with partial ring-opening under the neutral processing conditions employed, in agreement with the literature on AKD–cellulose reactions [36, 37]. The incorporation of HNT is evidenced by the progressive enhancement and broadening of peaks in the 1000–1100 cm^{-1} region, corresponding to Si—O—Si asymmetric stretching. Additional features at ~900–950 cm^{-1} (Al—O vibrations) and ~470–500 cm^{-1} (Si–O bending) become more pronounced with increasing HNT content, confirming successful integration of the inorganic phase [38]. Furthermore, the appearance of bands at ~3695 and ~3620 cm^{-1}, assigned to inner surface hydroxyl groups of halloysite, provides additional evidence of HNT presence [38, 39]. Notably, a reduction in the intensity of the O—H stretching band (~3330 cm^{-1}) is observed after modification, indicating partial surface coverage of NFC hydroxyl groups by AKD and interaction with HNT. At the same time, slight broadening of this region suggests the formation of new hydrogen-bonding interactions among NFC, AKD, and HNT components. The systematic increase in intensity of HNT-related bands with increasing loading (NFC (i), NAH1 (ii), NAH5 (ii), NAH10 (iii), 1-10 wt.%) confirms their uniform incorporation within the NFC matrix.

Figure 2b shows the XRD patterns of neat NFC and nanocomposite foams. The neat NFC exhibits characteristic diffraction peaks at approximately 16.2°, 23.1°, and 34.4°, corresponding to the (110), (200), and (004) lattice planes of cellulose I, consistent with the well-established crystalline structure of nanocellulose [32–34]. After incorporation of AKD and HNT, the main cellulose I diffraction peaks remain clearly visible, demonstrating that the crystalline structure of NFC is preserved during composite formation. This indicates that the freeze-drying process and HNT nanofiller incorporation do not induce any phase transformation, in agreement with previous reports on cellulose-based nanocomposites [40]. However, a gradual decrease in the intensity and slight broadening of the (200) peak is observed with increasing HNT content. This suggests a partial reduction in long-range ordering of the cellulose chains, likely due to interfacial interactions between NFC and the HNT, as well as disruption of the native hydrogen-bonding network. Similar trends have been reported in other cellulose-based hybrid systems upon incorporation of nanofillers [41]. In addition to the cellulose peaks, new diffraction features appear at ~12.2°, 20.4°, 35.2–38.4°, 54.9°, and ~62.4°, which are characteristic of HNT nanotubes with an aluminosilicate layered structure. The progressive increase in intensity of these peaks with increasing HNT (NAH1 to NAH10) loading confirms the successful incorporation of HNT within the NFC matrix [42]. The absence of significant peak shifts or additional reflections suggests that HNT is physically integrated rather than chemically altering the cellulose crystalline phase [43].

Overall, the XRD results confirm that the nanocomposite foams retain the cellulose I crystalline framework while incorporating crystalline halloysite nanotubes. The observed changes in peak intensity and broadening reflect interfacial interactions and partial disruption of cellulose ordering, which are expected to influence the mechanical, thermal, and flame-retardant properties of the resulting materials.

2.3 | Morphology and Microstructural Features of Nanocomposite Foams

The microstructural features of neat NFC and NFC–AKD–HNT nanocomposite foams were investigated by SEM (Figure 3) and complemented by EDX elemental mapping (Figure S3). The neat NFC foam exhibits the typical morphology of freeze-dried nanocellulose aerogels, consisting of an interconnected 3D porous network with large macropores (50–250 μm, occasionally up to ~300 μm) and thin fibrillar walls [10, 44]. At higher magnification (Figure 3a,b and Figure S4), a loosely entangled network of cellulose nanofibrils is observed, forming ultrathin junctions that contribute to high porosity and low density [5]. Upon incorporation of 1 wt.% HNT (NAH1), the porous architecture is largely preserved, with a similar pore size range (50–220 μm) and no evident pore closure. SEM images show that halloysite nanotubes are well dispersed along the fibrillar network, acting as nanoscale reinforcements without disrupting pore connectivity. This is further supported by EDX mapping (Figure S3), which reveals a homogeneous spatial distribution of Al and Si elements (characteristic of HNT) across the foam matrix, confirming uniform filler incorporation at low loading. At 5 wt.% HNT (NAH5), a clear structural evolution is observed. The pore walls become thicker and more consolidated, while the pore size distribution narrows (~40–180 μm), indicating enhanced structural integrity. High-magnification images (Figure S5) reveal localized clustering

16136829, 0, Downloaded from https://onlinelibrary.wiley.com/doi/10.1002/smll.75920 by Dtsch Zentrum F. Luft-U. Raum Fahrt In D. Helmholtz Gemein., Wiley Online Library on [27/09/2026]. See the Terms and Conditions (https://onlinelibrary.wiley.com/terms-and-conditions) on Wiley Online Library for rules of use; OA articles are governed by the applicable Creative Commons License

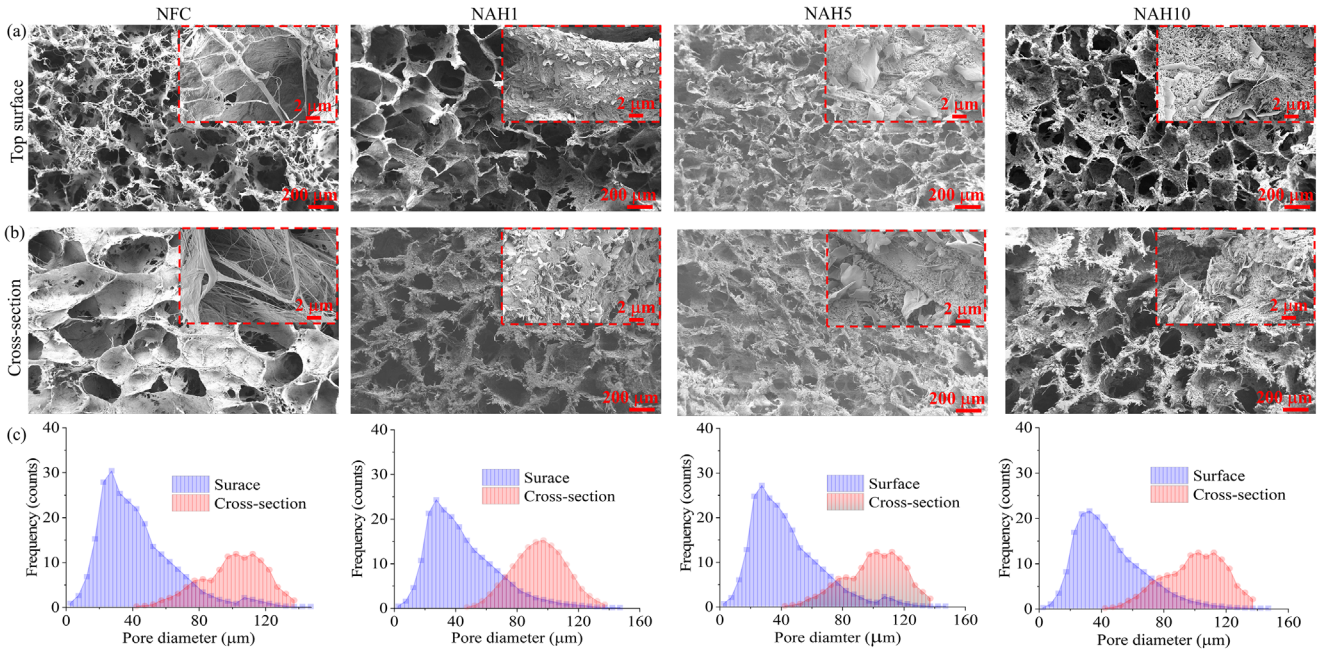


FIGURE 3 | SEM images and pore size distribution analysis of NFC foams and NFC–HNC–AKD nanocomposite foams. SEM images of the top surfaces (a) and cross-sections (b) are shown for NFC, NAH1, NAH5, and NAH10 foams. The red dashed boxes indicate higher-magnification regions highlighting the detailed microstructure of the pore walls. (c) Corresponding pore-size distribution profiles obtained from the surface and cross-sectional images.

of HNT and possible AKD-mediated bridging between fibrils, forming a more continuous network. Importantly, EDX elemental maps show increased intensity yet still relatively uniform distribution of Al and Si signals, suggesting effective dispersion with limited aggregation. This hierarchical organization supports improved interfacial interactions and mechanical reinforcement while maintaining interconnected porosity, consistent with previous reports on cellulose–clay composites [45]. In contrast, at higher loading (10 wt.% HNT, NAH10), the nanofoam structure becomes significantly denser. The pore walls are markedly thickened, and pore sizes decrease to 30–120 μm, with partial pore constriction and collapse. SEM images reveal the formation of clay-rich domains and reduced visibility of individual nanofibrils, indicating nanotube aggregation. This is corroborated by EDX mapping, where Al and Si signals appear more localized and heterogeneous, confirming the formation of aggregated regions at high filler content. Such aggregation leads to increased solid fraction, reduced pore accessibility, and structural coalescence, as commonly observed in cellulose–clay systems [46, 47]. The pore size distribution analysis (Figure 3c), derived from both surface and cross-sectional images, further supports these observations. NFC and NAH1 exhibit broad distributions dominated by large, open pores. NAH5 shows a slightly narrower and more uniform distribution, reflecting improved wall stability, while NAH10 exhibits a narrower distribution with smaller pores, consistent with densification and partial pore closure.

Lateral cross-sectional SEM images (Figure S6) reveal composition-dependent differences in pore structural orientation. Neat NFC and NAH1 display moderately elongated macropores and partially aligned fibrillar structure along the freeze-drying axis, reflecting the directional ice crystal growth during freeze-drying. This directional alignment is most pronounced in NAH5, which exhibits clearly elongated and preferentially oriented pore channels and fibrillar wall structures. In contrast, NAH10 shows a denser and more isotropic pore arrangement, reflecting the progressive disruption of directional pore architecture by partial HNT aggregation at high loading. This composition-dependent structural gradient provides direct morphological evidence for the anisotropic thermal conductivity behavior discussed in Section 2.6.3, where the degree of anisotropy decreases with increasing HNT content.

SEM images (see Figure S7) of the combustion residues reveal a marked change in char morphology upon HNT incorporation. In contrast to neat NFC, which leaves a more fragile and porous residue, the HNT-containing nanofoams (NAH1 and NAH10) form a progressively denser, more cohesive, and continuous char layer after burning. This morphological evolution supports the proposed barrier effect of HNT, which likely reduces heat transfer and limits the escape of volatile degradation products during combustion (see section 2.6). The more compact residue observed at higher HNT loading (NAH10) suggests improved char stabilization and structural integrity, thereby contributing to the observed self-extinguishing behavior. However, as SEM is a morphological method, it does not directly evidence phase transitions within the char layer; therefore, the present discussion is restricted to structural interpretation.

Altogether, the combined SEM and EDX analyses demonstrate that halloysite loading plays a critical role in tailoring the microstructure of NFC-based nanofoams. Low HNT content preserves the intrinsic porous architecture, moderate loading (5 wt.%) yields a hierarchically reinforced yet highly porous network with uniform filler dispersion, and excessive loading leads to structural densification due to nanotube aggregation.

16136829, 0, Downloaded from https://onlinelibrary.wiley.com/doi/10.1002/smll.75920 by Dtsch Zentrum F. Luft-U. Raum Fahrt In D. Helmholtz Gemein., Wiley Online Library on [27/09/2026]. See the Terms and Conditions (https://onlinelibrary.wiley.com/terms-and-conditions) on Wiley Online Library for rules of use; OA articles are governed by the applicable Creative Commons License

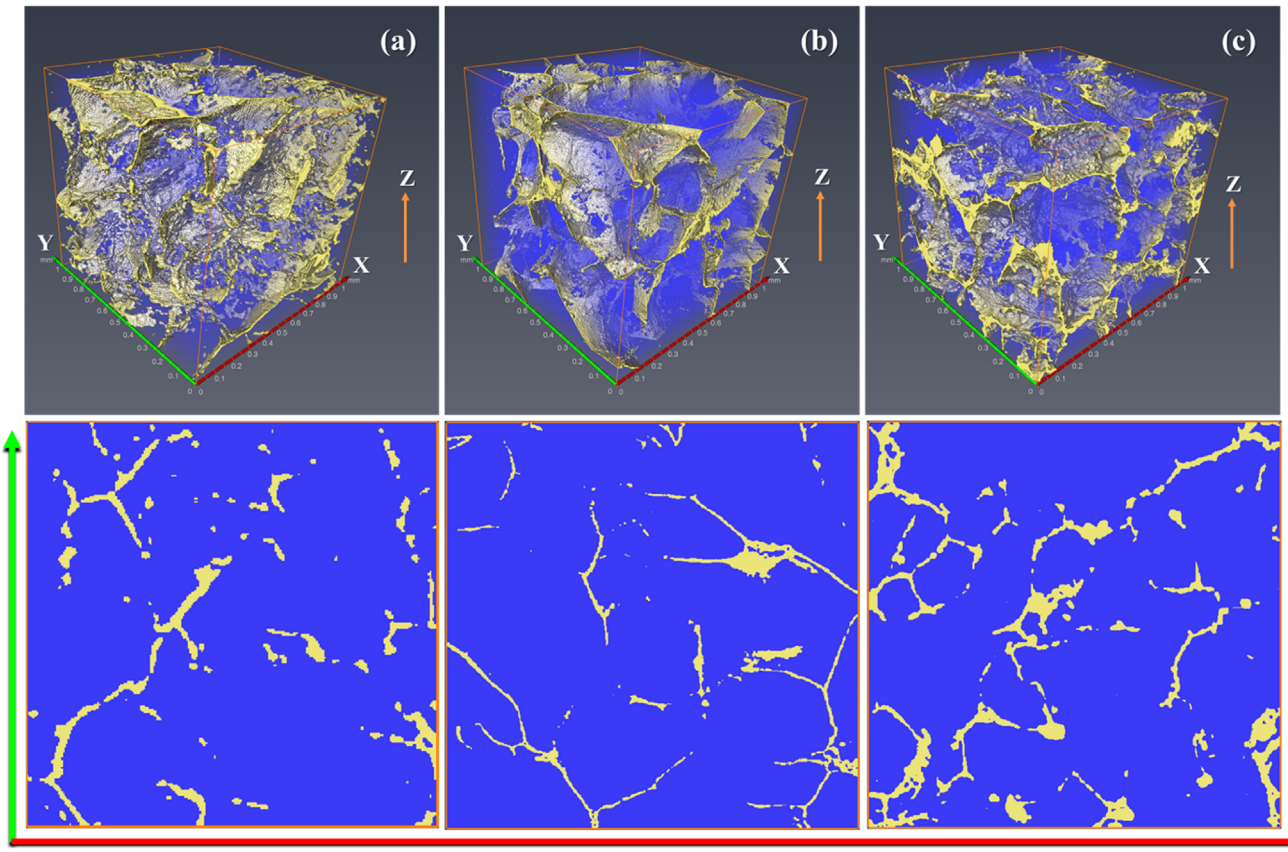


FIGURE 4 | μ-CT images of neat NFC (a), NAH1 (b), and NAH10 (c) foams. The 2D cross sectional images (bottom row) show the dimensions of the solid distributed in the middle of the reconstructed volume (from the corresponding 3D images represented in the top row).

TABLE 1 | Results of the statistical analysis of μ-CT data obtained from neat NFC and NFC-AKD-HNT nanocomposite foams.

Sample name	Volume fraction of air (%)	Volume fraction of solid (%)	Area of solid per cubic millimeter (mm^2)
NFC	93.5	6.5	13.5172
NAH1	96.1	3.9	13.3032
NAH10	89.3	10.7	18.9558

Among the compositions studied, NAH5 provides the most favorable balance between structural integrity, porosity, and filler distribution, which is expected to directly influence the thermal, mechanical, and flame-retardant performance of the nanocomposite foams.

μ-CT was employed to investigate the 3D internal architecture of the NFC-based foams and to complement SEM observations. The reconstructed 3D volumes (Figure 4, top row) and corresponding central cross-sections (bottom row) provide non-destructive insight into the spatial distribution and connectivity of the solid framework within the porous matrix. In the segmented images, the solid phase is shown in yellow and the pore space in blue, clearly visualizing the interconnected network. The neat NFC foam (Figure 4a) exhibits a highly porous, open-cell structure composed of a sparse network of thin, interconnected struts enclosing large voids. Quantitative μ-CT analysis (Table 1) confirms this architecture, with a porosity of 93.5% and a solid volume fraction of 6.5%. The structure thickness (0.027 ± 0.0003 mm) and large structure separation (0.551 ± 0.018 mm) indicate thin walls and large pores, while the low specific surface area (0.197 ± 0.007 mm^{-1}) reflects the highly open and lightweight nature of the foam. These results are consistent with SEM observations of an entangled nanofibrillar network forming thin walls and large macropores. With the incorporation of 1 wt.% HNT (NAH1), subtle structural changes are observed. The 3D reconstructions (Figure 4b) show a more continuous and slightly densified network while maintaining high porosity (96.2 ± 0.1%). The solid volume fraction increases to 3.8 ± 0.1%, structure thickness to 0.033 ± 0.0007 mm, and structure separation decreases to 0.437 ± 0.013 mm. The specific surface area also increases to 0.250 ± 0.010 mm^{-1}, indicating a more refined and interconnected structure. These changes suggest that low HNT loading reinforces the cellulose framework by thickening pore walls and improving connectivity without compromising porosity, consistent with SEM observations and literature reports. At higher loading (10 wt.% HNT, NAH10), more pronounced structural evolution occurs. The solid volume fraction increases to 10.7%, structure thickness

16136829, 0, Downloaded from https://onlinelibrary.wiley.com/doi/10.1002/smll.75920 by Dtsch Zentrum F. Luft-U. Raum Fahrt In D. Helmholtz Gemein., Wiley Online Library on [27/09/2026]. See the Terms and Conditions (https://onlinelibrary.wiley.com/terms-and-conditions) on Wiley Online Library for rules of use; OA articles are governed by the applicable Creative Commons License

TABLE 2 | Results of the density, BET isotherm, and static water contact angle analysis of neat NFC and NFC-AKD-HNT nanocomposite foams.

Samples	Density (g mL^{-1})	Specific surface area (m^2 g^{-1})	Pore volume (cm^3 g^{-1})	Pore size (nm)	SCA (H_2O)°
NFC	0.0865	5.444 ± 0.9	0.0127 ± 0.003	9.2 ± 1.1	0
NAH1	0.0668	9.572 ± 0.04	0.031 ± 0.001	12.7 ± 0.2	133 ± 3
NAH5	0.1592	16.931 ± 0.5	0.075 ± 0.002	17.8 ± 0.2	140 ± 5
NAH10	0.3521	20.1 ± 0.7	0.095 ± 0.002	18.9 ± 0.1	154 ± 6

to 0.034 ± 0.0006 mm, and structure separation decreases to 0.340 ± 0.008 mm, while the specific surface area reaches 0.289 ± 0.004 mm^{-1}. The 3D renderings reveal thicker and more clustered solid domains, and cross-sections show localized densification. These observations align with SEM results showing thicker pore walls and halloysite aggregation, indicating partial structural coalescence at higher filler content, a behavior commonly reported in cellulose–clay systems [46, 48]. Importantly, μ-CT parameters correlate closely with SEM-based pore size analysis. The decrease in structure separation from NFC (0.551 mm) to NAH1 (0.437 mm) and NAH10 (0.340 mm) mirrors the reduction in pore size observed in SEM. Similarly, increases in structure thickness and solid volume fraction are consistent with wall thickening and clay-rich domains. This agreement confirms the reliability of the structural interpretation across length scales.

The combined μ-CT and SEM analyses reveal a clear composition-dependent evolution of the foam architecture: neat NFC forms an ultralight, open network; low HNT loading (NAH1) provides reinforcement while preserving porosity; and higher loading (NAH10) leads to partial densification due to nanotube aggregation. These results highlight the critical role of nanofiller content in tuning pore structure and connectivity, ultimately governing the thermal, mechanical, and flame-retardant performance of the foams.

2.4 | Bulk Density, Porous Structure and Wettability Analysis of Nanocomposite Foams

The bulk structural properties of neat NFC and nanocomposite foams were further evaluated by density and BET analysis, as summarized in Table 2. These measurements provide quantitative insight into surface area, pore volume, and mesoporous characteristics, complementing the macroscopic structural information obtained from SEM and μ-CT. The neat NFC foam exhibits a low density of 0.0865 g mL^{-1}, consistent with its highly porous aerogel-like structure [9, 44]. It shows a BET surface area of 5.44 ± 0.9 m^2 g^{-1}, a pore volume of 0.0127 ± 0.003 cm^3 g^{-1}, and an average pore diameter of 9.2 ± 1.1 nm. The relatively low BET surface area and pore volume indicate that the porosity is dominated by macropores, which are not fully captured by nitrogen adsorption. This is in good agreement with SEM and μ-CT results, which revealed large, interconnected pores and a sparse fibrillar network. Such behavior is typical of freeze-dried nanocellulose aerogels, where macroporosity governs the structure while BET-accessible surface area remains modest [5, 18, 44]. For NAH1, the density slightly decreases to 0.0668 g mL^{-1}, suggesting improved structural expansion or stabilization during freeze-drying. In contrast, the BET surface area nearly doubles to 9.57 ± 0.04 m^2 g^{-1}, accompanied by an increase in pore volume (0.031 ± 0.001 cm^3 g^{-1}) and average pore diameter (12.7 ± 0.2 nm). This indicates that well-dispersed HNT introduces additional accessible internal surfaces and promotes the formation of mesopores. These findings are consistent with SEM and μ-CT observations, where HNT was uniformly distributed along cellulose fibrils, enhancing structural connectivity without blocking pores. At NAH5, a more pronounced structural evolution is observed. The density increases to 0.1592 g mL^{-1}, indicating a higher solid fraction within the foam. Correspondingly, the BET surface area increases to 16.93 ± 0.5 m^2 g^{-1}, with a pore volume of 0.075 ± 0.002 cm^3 g^{-1} and an average pore diameter of 17.8 ± 0.2 nm. These results suggest the development of a more complex hierarchical pore structure with increased mesoporosity and internal surface area. SEM and μ-CT analyses support this interpretation, showing thicker pore walls and improved structural continuity. Together, these findings indicate that moderate HNT loading effectively enhances the internal surface structure while preserving an interconnected porous network. In the case of NAH10, the density increases significantly to 0.3521 g mL^{-1}, reflecting substantial incorporation of inorganic content. The BET surface area reaches 20.1 ± 0.7 m^2 g^{-1}, with a pore volume of 0.095 ± 0.002 cm^3 g^{-1} and an average pore diameter of 18.9 ± 0.1 nm. While the continued increase in surface area and pore volume confirms the contribution of HNT to mesoporosity, SEM and μ-CT results reveal clear signs of structural densification and partial nanotube aggregation. The formation of thicker pore walls and clay-rich domains suggests that excessive filler loading leads to localized coalescence, a behavior commonly reported in cellulose–clay aerogels [45].

Overall, the combined density and BET analyses reveal a composition-dependent transition from a macropore-dominated structure (NFC) to a hierarchical macro–mesoporous architecture (NAH1–NAH10). The progressive increase in surface area, pore volume, and mesopore size reflects the dual role of HNT as both a structural reinforcement and a mesopore-generating agent. When correlated with SEM and μ-CT observations, these results confirm that moderate HNT loading optimizes the balance between porosity and structural integrity, while excessive loading leads to densification and reduced pore accessibility.

The surface wettability of the nanocomposite foams was evaluated using static water contact angle (SCA(H_2O)) measurements (Table 2). Except for neat NFC, all samples exhibit contact angles above 90°, confirming hydrophobic behavior. Notably, NFC–AKD samples (without HNT, data not shown) already show high contact angles (~134°), demonstrating that AKD is the primary factor governing hydrophobicity by effectively lowering the surface energy of the cellulose network. Upon incorporation of HNT, the

16136829, 0, Downloaded from https://onlinelibrary.wiley.com/doi/10.1002/smll.75920 by Dtsch Zentrum F. Luft-U. Raum Fahrt In D. Helmholtz Gemein, Wiley Online Library on [27/09/2026]. See the Terms and Conditions (https://onlinelibrary.wiley.com/terms-and-conditions) on Wiley Online Library for rules of use; OA articles are governed by the applicable Creative Commons License

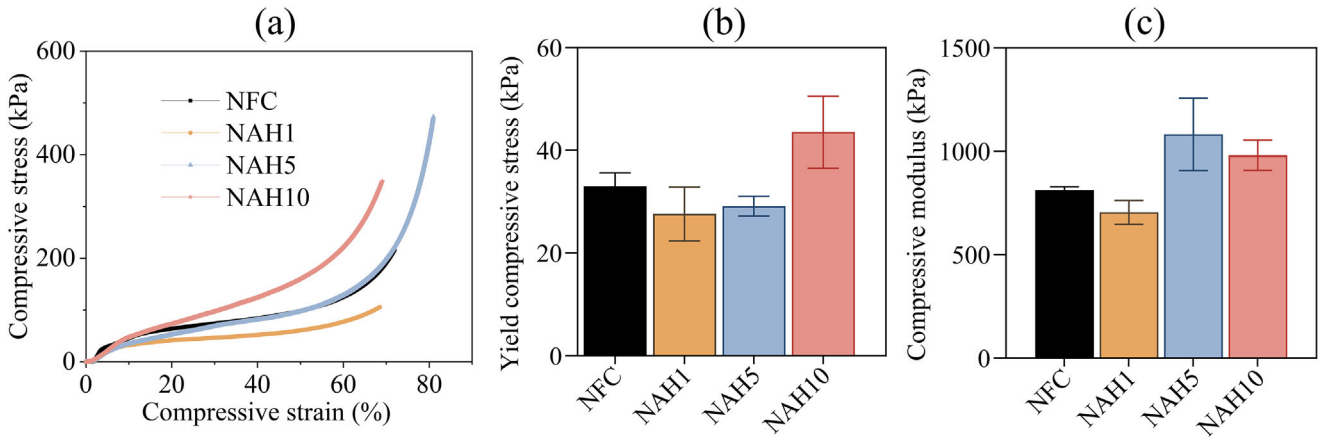


FIGURE 5 | (a) stress–strain curves (b) compressive (plateau) stress of the samples, and (c) Young's modulus of neat and NAH nanocomposite foams.

SCA values remain within 133 ± 5° to 154 ± 11°, indicating that HNT does not significantly alter the intrinsic surface chemistry but instead plays a secondary, structural role. Importantly, the hydrophobicity remains stable over time. Samples stored under ambient conditions for over six years exhibit contact angles comparable to initial values (Figure S8), confirming the long-term durability of the AKD-modified surface. This stability indicates that the hydrophobic layer is chemically robust and resistant to environmental degradation. SEM images of the NFC–AKD foam (without HNT) are provided in Figure S9. Direct comparison with neat NFC (Figure 3 and Figure S4) shows that the open-cell macroporous network and pore size distribution (50–250 μm) are fully preserved after AKD treatment, with no evidence of pore collapse, wall thickening, or structural densification. This confirms that AKD acts exclusively as a surface modifier and does not disrupt the hierarchical porous architecture. At the same time, (SCA(H_2O)) of 134 ± 3° for NFC–AKD foams compared to ~0° for unmodified neat NFC confirm that hydrophobization is achieved by surface chemistry rather than by pore filling or blockage, allowing the hierarchical architecture required for efficient thermal insulation to be preserved.

2.5 | Mechanical Properties

The uniaxial compressive mechanical properties of the nanocomposite foams were evaluated through stress–strain analysis (Figure 5a). Assessing compressive behavior is critical for porous foams, as it determines their ability to withstand mechanical loads, maintain structural integrity, and function reliably in applications such as insulation, packaging, and energy absorption. All samples exhibit characteristic J-shaped stress–strain curves typical of cellular solids, indicating their ability to sustain large deformations without catastrophic failure [49]. The response can be divided into three regimes: an initial elastic region (<20% strain) associated with pore wall bending, a plateau region (20%–60% strain) dominated by cell wall buckling, and a densification regime (>60% strain) marked by a sharp stress increase due to pore collapse [49, 50]. In addition, a clear composition-dependent reinforcement effect is observed with increasing HNT content. The neat NFC foam shows the lowest compressive strength (~200 kPa at ~70%–80% strain), while HNT incorporation significantly enhances the load-bearing capability. Among the composites, NAH5 exhibits the highest compressive strength (~480–500 kPa), followed by NAH10 (~350 kPa) and NAH1 (~100 kPa). This indicates that moderate HNT loading (5 wt%) provides the most effective reinforcement, whereas excessive loading (10 wt%) reduces mechanical efficiency, likely due to nanotube aggregation and stress concentration effects [51, 52]. The extracted mechanical parameters further support this trend. The yield stress increases overall with HNT incorporation, reaching the highest value for NAH10 (~45 kPa), although NAH5 maintains superior performance at higher strains (Figure 5b). Similarly, the compressive modulus (Figure 5c) shows a non-monotonic trend, increasing from ~800 kPa (NFC) to a maximum of ~1100 kPa (NAH5), followed by a slight decrease for NAH10 (~1000 kPa). These results suggest that while higher HNT filler loading improves initial stiffness and yield resistance, it can compromise structural uniformity and load transfer at larger deformation [51]. The observed mechanical enhancement is attributed to the tubular morphology of HNT, which acts as a rigid reinforcing phase within the NFC network. At optimal loading (NAH5), well-dispersed nanotubes reinforce the fibrillar structure through mechanical interlocking and interfacial interactions, enabling efficient stress transfer [51, 53]. This is consistent with SEM and μ-CT results, which show thicker pore walls and increased structural connectivity. In contrast, higher HNT content leads to partial aggregation, resulting in localized heterogeneities and reduced mechanical efficiency. The mechanical behavior also correlates with density and BET results, where increasing HNT content leads to higher solid fraction and internal surface area. While increased density contributes to improved stiffness, excessive filler incorporation reduces structural uniformity, highlighting a balance between reinforcement and porosity.

Compared with the literature, the NAH5 foam (~1100 kPa modulus and ~500 kPa compressive strength) demonstrates competitive or superior performance relative to typical nanocellulose aerogels (300–800 kPa) and cellulose–clay composites (~600–1000 kPa). Moreover, unlike brittle synthetic foams (e.g., polystyrene), which fail at low strain, the NFC–HNT foams maintain structural integrity up to ~70%–80% strain, indicating excellent compressibility and energy absorption capability.

16136829, 0, Downloaded from https://onlinelibrary.wiley.com/doi/10.1002/smll.75920 by Dtsch Zentrum F. Luft-U. Raum Fahrt In D. Helmholtz Gemein., Wiley Online Library on [27/09/2026]. See the Terms and Conditions (https://onlinelibrary.wiley.com/terms-and-conditions) on Wiley Online Library for rules of use; OA articles are governed by the applicable Creative Commons License

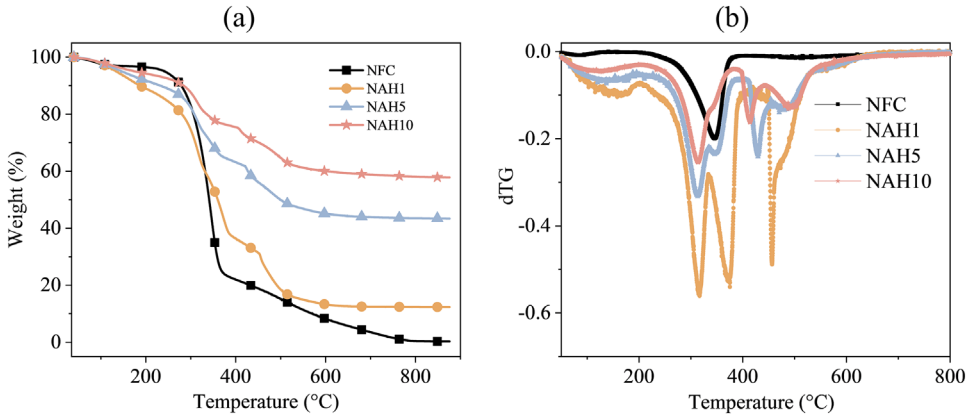


FIGURE 6 | (a) Thermogravimetric analysis (TGA) curves and (b) corresponding derivative thermogravimetric (dTG) curves of neat NFC and NAH nanocomposite foams.

Overall, these results demonstrate that halloysite nanotubes play a critical role in tailoring the mechanical performance of NFC-based foams. Moderate loading (5 wt%) provides the optimal balance between stiffness, strength, and deformability, making these materials promising candidates for lightweight structural and energy-absorbing applications.

2.6 | Thermal Stability, Flame Retardancy, Thermal Insulation, and Heat Transport Properties of Nanocomposite Foams

2.6.1 | Thermal Stability Analysis

The thermal degradation behavior of neat NFC and NAH nanocomposite foams was analyzed by TGA and its derivative (dTG), revealing the characteristic multi-stage decomposition of cellulose-based materials (Figure 6). All samples exhibit three distinct degradation stages. The initial stage (<100°C–120°C) corresponds to ~5%–10% mass loss due to the evaporation of physically adsorbed water. The second stage (~200°C–300°C) marks the onset of thermal degradation, involving dehydration reactions and cleavage of less stable bonds. The third and dominant stage (~300°C–380°C) is associated with rapid cellulose depolymerization and glycosidic bond scission, accounting for the major mass loss (~40%–60%), consistent with previous studies on cellulose thermal degradation mechanisms [34, 54]. At higher temperatures (>400°C), gradual decomposition of carbonaceous residues occurs, leaving significant char yields (~25%–45% at 800°C), indicative of enhanced thermal stability and fire-retardant potential [55]. The dTG curves (Figure 6b) provide further insight into degradation kinetics. Neat NFC exhibits a sharp DTG peak at ~320°C (T_{max}), reflecting rapid decomposition [32, 33]. In contrast, HNT-containing samples display broader and less intense peaks with slight shifts toward higher temperatures (~330°C–350°C), indicating a reduced degradation rate and more gradual decomposition. This behavior indicates that HNT alters the degradation pathway by limiting the release of volatile degradation products and promoting the formation of thermally stable intermediate and char structures. Notably, the residual mass increases systematically with HNT content (NAH10> NAH5> NAH1> NFC), confirming the role of HNT in enhancing thermal resistance through its inorganic aluminosilicate nature and its ability to promote char formation [26]. The improved thermal stability arises from synergistic mechanisms, including (i) a barrier effect that restricts heat transfer and volatile diffusion, (ii) physical confinement of cellulose chains that reduces molecular mobility, and (iii) formation of a stable protective char layer that limits further degradation [25]. In comparison, the role of AKD is secondary; while it may slightly influence the initial degradation onset through modification of hydrogen bonding, the overall thermal behavior is predominantly governed by HNT incorporation and dispersion. At moderate loading, well-dispersed HNT provides efficient reinforcement and barrier effects, whereas higher loading may lead to partial aggregation. Nevertheless, the dominant effect is the formation of a stable char layer, which slows mass loss and enhances thermal stability. It can be suggested that HNT effectively modifies the degradation mechanism, resulting in reduced mass loss rates, broadened decomposition profiles, and enhanced char formation. These features, together with the hierarchical structure of the foams, underline their potential for thermally stable and fire-resistant applications.

2.6.2 | Flame Retardancy and Combustion Behavior

The flame-retardant performance of the nanocomposite foams was evaluated using horizontal and vertical flammability tests, and the results are shown in Figure 7a,b. A clear enhancement in fire resistance is observed upon incorporation of AKD and HNT into the NFC matrix. The neat NFC foam ignites rapidly and undergoes complete combustion, leaving negligible residue, which is consistent with the inherent flammability of cellulose [5, 15]. This is reflected in its high combustion velocity (~6 cm s^{-1}), indicating rapid flame propagation. A more pronounced improvement is achieved with the incorporation of HNT. Even at low loading (NAH1), the foams exhibit immediate self-extinguishing behavior, with combustion confined near the ignition zone. The combustion velocity decreases significantly to ~1.3 cm s^{-1}, representing a substantial reduction compared to neat NFC. With increasing HNT content, flame retardancy is further enhanced: NAH5 and NAH10 exhibit very low combustion velocities (~0.3–0.4 cm s^{-1} and ~0.1–0.2 cm s^{-1}, respectively). At higher loadings, flame propagation is effectively suppressed, and the structural integrity of the foams is largely preserved, as evidenced by

16136829, 0, Downloaded from https://onlinelibrary.wiley.com/doi/10.1002/smll.75920 by Dtsch Zentrum F. Luft-U. Raum Fahrt In D. Helmholtz Gemein., Wiley Online Library on [27/09/2026]. See the Terms and Conditions (https://onlinelibrary.wiley.com/terms-and-conditions) on Wiley Online Library for rules of use; OA articles are governed by the applicable Creative Commons License

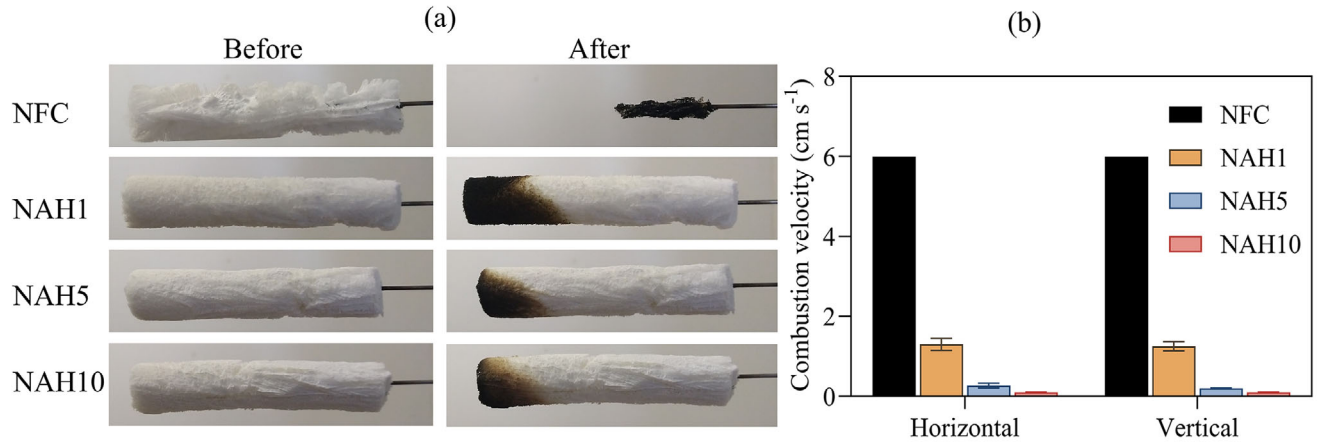


FIGURE 7 | Evaluation of flame retardancy and thermal insulation performance of NFC and NFC–AKD–HNT nanocomposite foams. (a) Digital images of the samples before and after flame exposure, (b) Combustion velocity measured under horizontal and vertical configurations.

minimal burned length and retained morphology. Importantly, similar trends are observed in both horizontal and vertical configurations, indicating that the improved fire resistance is governed by intrinsic material properties rather than orientation effects. The enhanced flame retardancy can be attributed to multiple synergistic mechanisms. Halloysite nanotubes (HNT) act as thermally stable inorganic barriers, limiting heat transfer and restricting the diffusion of oxygen and volatile degradation products [26, 39, 52]. In addition, increased char formation, as confirmed by TGA analysis, leads to the formation of a protective carbonaceous layer that insulates the underlying material. The tubular morphology of HNT further promotes the formation of a continuous and mechanically stable char network. AKD contributes indirectly by imparting hydrophobicity (contact angle >130°), reducing moisture uptake and stabilizing the structure under thermal exposure. These results strongly correlate with the previously observed structural (SEM/μ-CT) and thermal (TGA/DTG) properties, highlighting a clear structure–property relationship. Reinforced pore walls, increased solid fraction, and enhanced char formation collectively contribute to suppressed flame propagation and improved fire resistance.

Compared with the literature, neat nanocellulose aerogels typically exhibit rapid flame spread and negligible char residue, while the addition of inorganic fillers generally provides only moderate improvement [5, 56]. In contrast, the present NFC–AKD–HNT system demonstrates near self-extinguishing behavior and significantly reduced combustion velocities, even at low filler loadings, without the use of toxic flame-retardant additives. These findings demonstrate that the synergistic combination of hierarchical structure, inorganic reinforcement, and surface modification enables efficient flame suppression while preserving the lightweight and porous nature of the foam. This positions the NFC–AKD–HNT nanocomposite foams as promising candidates for sustainable, fire-safe thermal insulation applications.

2.6.3 | Thermal Insulation and Thermal Conductivity

Infrared thermography was used to evaluate the thermal insulation performance of the nanocomposite foams under continuous heat exposure (Figure 8a,b). Thermal images recorded at 0 and 15 min reveal clear, composition-dependent differences in heat accumulation. At the initial stage, all samples exhibit similar surface temperatures (~30°C–35.4°C), indicating comparable starting conditions. After 15 min, the neat NFC sample reaches ~46.8°C, while AKD- and HNT-containing foams show slightly higher steady-state temperatures (~47.0°C–48.4°C). The overall temperature increase ($\Delta T \approx 13°C–17°C$) remains relatively narrow, confirming that all samples retain effective thermal insulation. The slightly higher temperatures observed for HNT-containing foams indicate a modest increase in heat transfer, attributed to the introduction of inorganic nanotubes that act as additional solid-phase conduction pathways [5, 57]. Nevertheless, heat remains highly localized at the heating zone with minimal lateral spreading, indicating that heat transport is dominated by through-thickness conduction, characteristic of highly porous cellular materials [58]. The insulation performance primarily arises from the hierarchical porous structure of the NFC network, which traps air within micro- and nanoscale pores and suppresses conductive and convective heat transfer [9, 56]. The incorporation of HNT introduces a trade-off: while slightly increasing heat transfer, it significantly enhances mechanical strength and flame retardancy. These findings are consistent with infrared thermography studies of porous bio-based and hybrid insulation materials. Nanocellulose aerogels and cellulose foams typically exhibit surface temperature increases of ~10°C–20°C under similar conditions, depending on density and pore structure [59, 60]. Likewise, polymer–clay and cellulose–clay composites often show slightly higher steady-state temperatures due to enhanced solid-phase heat conduction, while still maintaining localized heating and limited lateral heat spreading [4, 7, 45]. Compared to these systems, the present NFC–AKD–HNT foams demonstrate comparable thermal response while offering additional functionalities such as mechanical robustness, hydrophobicity, and improved flame retardancy.

The thermal conductivity of neat NFC and NFC–AKD–HNT nanocomposite foams was quantitatively measured in both radial and axial directions and is summarized in Figure 8b (right axis). The neat NFC foam exhibits low thermal conductivity values of 0.03449 ± 0.001 W m^{-1} K^{-1} (radial) and 0.0312 ± 0.001 W m^{-1} K^{-1} (axial), confirming its excellent insulation

16136829, 0, Downloaded from https://onlinelibrary.wiley.com/doi/10.1002/smll.75920 by Dtsch Zentrum F. Luft-U. Raum Fahrt In D. Helmholtz Gemein., Wiley Online Library on [27/09/2026]. See the Terms and Conditions (https://onlinelibrary.wiley.com/terms-and-conditions) on Wiley Online Library for rules of use; OA articles are governed by the applicable Creative Commons License

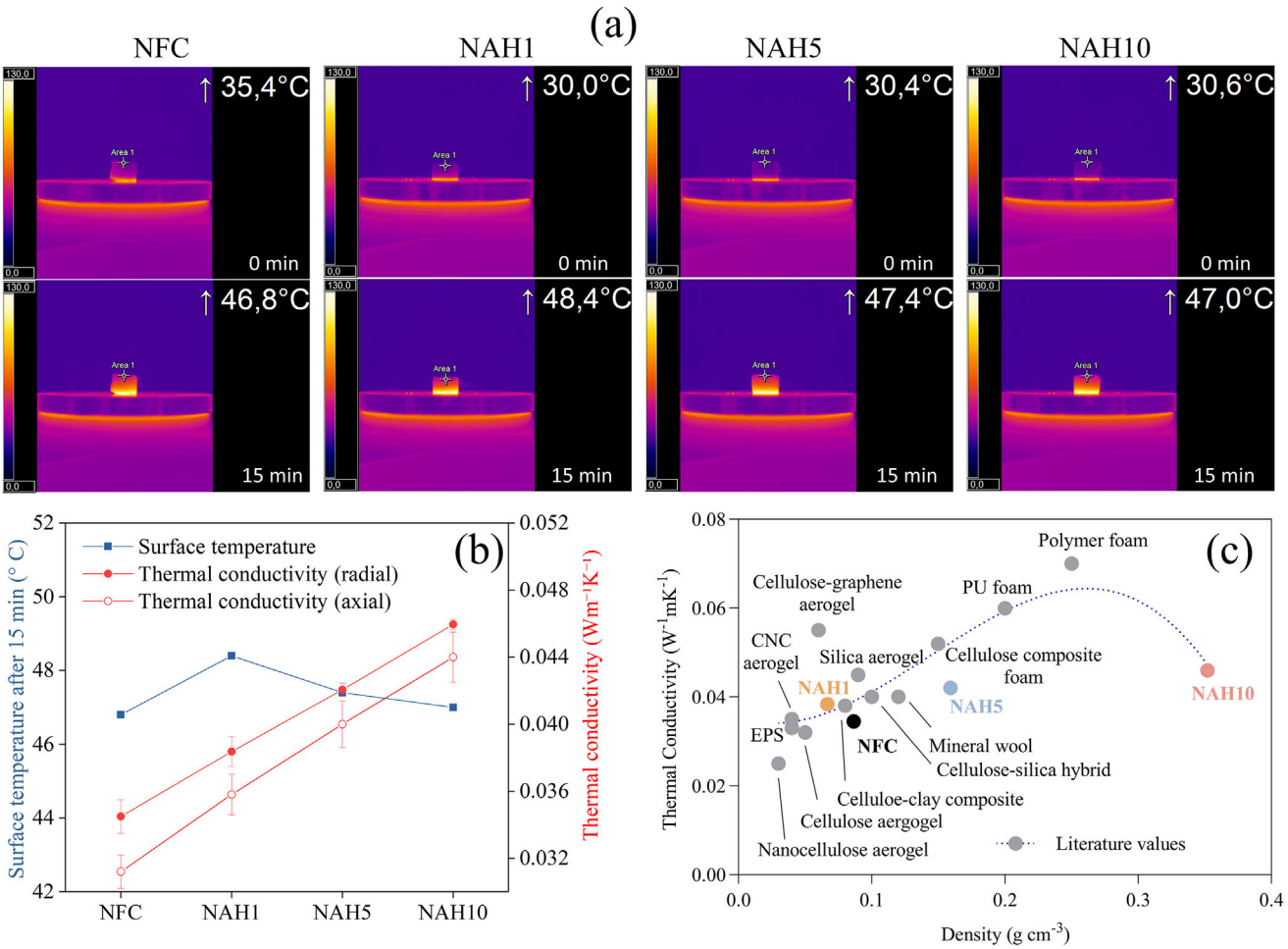


FIGURE 8 | (a) Infrared thermographic images recorded at 0 and 15 min during continuous heat exposure, (b) Surface temperature after 15 min of heat exposure (left axis) and Axial and radial thermal conductivity values (right axis), and (c). Density– thermal conductivity relationship of NFC–AKD–HNT nanofoams compared with literature porous materials.

capability. Upon incorporation of HNT, a gradual increase is observed in both directions. The radial thermal conductivity increases to 0.03836 ± 9 × 10^{-4} (NAH1), 0.04205 ± 4 × 10^{-4} (NAH5), and 0.04596 ± 3 × 10^{-4} W m^{-1} K^{-1} (NAH10), while the axial values follow a similar trend, reaching 0.0358 ± 0.0012, 0.040 ± 0.0014, and 0.044 ± 0.0015 W m^{-1} K^{-1}, respectively. This corresponds to moderate increases of approximately 11%–33%, depending on composition and direction. Notably, the axial thermal conductivity is consistently slightly lower than the radial values, suggesting a degree of anisotropic heat transport, likely arising from the directional alignment of the porous structure and fibrillar network formed during freeze-drying. The lower axial thermal conductivity compared to the radial direction can be rationalized by the partially aligned pore channels and fibrillar network oriented along the freeze-drying direction, as directly evidenced by the lateral cross-sectional SEM images in Figure S6. Importantly, the degree of thermal conductivity anisotropy, measured as the difference between radial and axial values, decreases progressively with HNT loading, from approximately 10% for neat NFC to ~7% for NAH1, ~5% for NAH5, and ~4% for NAH10. This trend is fully consistent with the SEM observations in Figure S6: directional pore elongation and fibrillar alignment are most pronounced in NFC and NAH5, while NAH10 displays a denser and more isotropic pore arrangement due to partial HNT aggregation at high loading, which disrupts the freeze-drying-induced directional architecture. Despite this anisotropy, both directions remain within the low thermal conductivity regime characteristic of high-performance insulating materials. This trend is consistent with the infrared thermography results, where HNT-containing samples exhibited slightly higher steady-state surface temperatures under heat exposure. Together, these findings confirm that halloysite incorporation leads to a controlled increase in heat transfer while preserving effective thermal insulation. The observed behavior can be rationalized using the effective thermal conductivity model:

$$\lambda_{\mathrm{eff}} = \lambda_{\mathrm{s}} + \lambda_{\mathrm{g}} + \lambda_{\mathrm{r}} \quad (1)$$

where heat transfer is governed by solid-phase conduction (λ_s), gas-phase conduction (λ_g), and a minor radiative contribution (λ_r). In neat NFC, the low thermal conductivity arises from its highly porous nanofibrillar network, which disrupts continuous solid pathways and suppresses gas-phase heat transfer via the Knudsen effect [61, 62], where heat transport becomes limited by molecule–wall collisions rather than intermolecular interactions

16136829, 0, Downloaded from https://onlinelibrary.wiley.com/doi/10.1002/smll.75920 by Dtsch Zentrum F. Luft-U. Raum Fahrt In D. Helmholtz Gemein., Wiley Online Library on [27/09/2026]. See the Terms and Conditions (https://onlinelibrary.wiley.com/terms-and-conditions) on Wiley Online Library for rules of use; OA articles are governed by the applicable Creative Commons License

[4]. In nanoscale pores, gas conductivity is reduced according to:

$$\lambda_{g,eff} = \frac{\lambda_{g,0}}{1 + \beta Kn} \quad (2)$$

where $\lambda_{g,\,eff}$ is the Effective gas-phase thermal conductivity inside the porous material ($Wm^{-1}K^{-1}$), $\lambda_{g,\,0}$ is the thermal conductivity of the free gas (air) under bulk conditions ($W{\cdot}m^{-1}{\cdot}K^{-1}$), at room temperature and pressure), β is an empirical coefficient ($\approx$ 1.5–2 for air), related to the energy transfer between gas molecules and the limiting solid structure, and K_n is the Knudsen number.

With increasing HNT content, the gradual rise in thermal conductivity is mainly attributed to an increase in the solid-phase contribution (λ_s). Halloysite nanotubes introduce thermally conductive inorganic pathways within the NFC matrix, facilitating phonon transport across pore walls. This is consistent with SEM and μ-CT observations, which show preserved porosity despite increased wall thickness and solid fraction. The role of AKD is secondary but beneficial; by imparting hydrophobicity (contact angle >150°), it reduces moisture uptake and prevents water-induced increases in thermal conductivity, thereby stabilizing performance under ambient conditions. From an application perspective, these results highlight a favorable balance between insulation and multifunctionality. While neat NFC provides the lowest thermal conductivity, HNT incorporation enhances mechanical strength, thermal stability, and flame retardancy with only a modest increase in heat transfer. Notably, NAH1 and NAH5 offer optimal performance, maintaining low thermal conductivity (radial: ~0.038–0.042 W m^{-1} K^{-1}; axial: ~0.036–0.040 W m^{-1} K^{-1}) while significantly improving structural and fire-resistant properties. Compared with literature, the thermal conductivity values fall well within the range reported for nanocellulose aerogels (~0.02–0.05 W m^{-1} K^{-1}), depending on density and pore structure [5, 15, 45, 58]. The modest increase with HNT addition is consistent with polymer–clay and cellulose–halloysite systems, where inorganic fillers slightly enhance solid-phase heat transport without compromising overall insulation performance [5, 45, 55].

The density–thermal conductivity relationship of the nanocomposite foams, together with representative porous materials from the literature, is presented in Figure 8c. All samples from this work (NFC, NAH1, NAH5, and NAH10) fall within the characteristic envelope of lightweight thermal insulators, confirming that the hierarchical porous architecture effectively suppresses heat transport. As the density increases from ~0.06 to ~0.35 g cm^{-3}, a gradual and monotonic increase in thermal conductivity is observed (from ~0.034 to ~0.046 W m^{-1} K^{-1}), which can be attributed to enhanced solid-phase conduction arising from thicker pore walls and increased solid volume fraction. Importantly, this trend follows a smooth scaling behavior without any abrupt transition, indicating that the system remains below the percolation threshold and retains a pore-dominated heat transfer regime. Such behavior is consistent with classical models for cellular solids and porous insulators, where thermal conductivity scales with density due to the increasing contribution of the solid network [4, 63][ref]. Compared with literature benchmarks, including CNF aerogels [18, 63], cellulose-based aerogels [5], silica aerogels [64], and conventional polymer foams such as polyurethane [65] and expanded polystyrene [66], the present nanocomposites occupy a highly competitive region in the density–conductivity space. In particular, the NAH series exhibits thermal conductivities within the typical range of nanocellulose aerogels (~0.02–0.05 W m^{-1} K^{-1}) [4, 25, 55] while simultaneously offering enhanced mechanical integrity and flame retardancy. This combination of properties is rarely achieved in conventional systems. Notably, polymer foams and composite foams generally exhibit higher thermal conductivities at comparable or higher densities [4, 45], while silica aerogels, despite their ultralow thermal conductivity (<0.02 W m^{-1} K^{-1}) [20, 64], are often limited by brittleness, high cost, and complex processing. In contrast, the present NFC–AKD–HNT nanofoams bridge this gap by combining low thermal conductivity with mechanical robustness, hydrophobic stability, and intrinsic flame resistance. The modest increase in thermal conductivity with halloysite incorporation further indicates that the addition of inorganic nanotubes does not disrupt the insulating regime but instead enables multifunctional enhancement without compromising performance.

To evaluate dimensional and structural stability under service-relevant thermal loading, representative foam compositions (NFC, NAH1, and NAH10) were subjected to 10 thermal cycles between room temperature (~25°C) and 80°C (1 h dwell at each temperature per cycle). After the full cycling program, macroscopic dimensions were unchanged within experimental error (<3%) for all compositions. For NAH10, the values remained essentially stable throughout: 0.046 W m^{-1} K^{-1} (cycle 0), 0.0462 W m^{-1} K^{-1} (cycles 1–3), 0.0465 W m^{-1} K^{-1} (cycles 4–6), and 0.0470 W m^{-1} K^{-1} (cycles 7–10) (Table S2), representing a cumulative change of ~2.2% over 10 cycles, within the instrument's measurement uncertainty ($\pm$ 3 × 10^{-4} W m^{-1} K^{-1}). SEM imaging of cross-sections of the same NAH10 sample (Figure S10) at room temperature before the first cycle (25°C, baseline) and after cooling to room temperature following the final 80°C dwell of cycle 10 confirmed that the hierarchical macroporous architecture, including pore size (50–250 μm) and fibrillar wall morphology, was fully preserved after the complete cycling program, with no evidence of pore collapse or structural densification (Figure S9). NFC and NAH1 foams showed similar behavior (see Table S2). Collectively, these results confirm that the air-filled pore space governing thermal insulation is not compromised by repeated thermal expansion and contraction, consistent with the TGA data (Section 2.6.1) showing that thermal degradation does not commence until well above 200°C, placing the 80°C cycling regime safely within the stable operating window of these materials.

Overall, these results demonstrate a favorable structure–property balance, where controlled increases in density and solid connectivity lead to predictable thermal behavior while maintaining effective insulation. This positions the NFC–AKD–HNT nanofoams within an optimal and previously underexplored performance window, highlighting their potential as next-generation sustainable thermal insulation materials.

3 | Conclusion

In this work, we present a hierarchically engineered NFC–AKD–HNT nanocomposite foam that successfully integrates

16136829, 0, Downloaded from https://onlinelibrary.wiley.com/doi/10.1002/smll.75920 by Dtsch Zentrum F. Luft-U. Raum Fahrt In D. Helmholtz Gemein., Wiley Online Library on [27/09/2026]. See the Terms and Conditions (https://onlinelibrary.wiley.com/terms-and-conditions) on Wiley Online Library for rules of use; OA articles are governed by the applicable Creative Commons License

thermal insulation, mechanical robustness, hydrophobicity, and intrinsic flame retardancy within a single bio-based system. By combining nanofibrillated cellulose with halloysite nanotubes and AKD surface modification, a multiscale structure–property design was achieved, enabling precise control over pore architecture, interfacial chemistry, and transport behavior. The results demonstrate that halloysite nanotubes play a dual role as structural reinforcements and functional fire-retardant agents. Their incorporation induces a transition from a purely macroporous NFC network to a hierarchical macro–mesoporous architecture, leading to enhanced mechanical performance (up to ∼1.1 MPa modulus), increased char formation (∼45%), and a dramatic reduction in combustion velocity (from ∼6 to ∼0.1 cm s^{-1}). At the same time, the materials maintain low thermal conductivity (0.034–0.046 W m^{-1} K^{-1}) and exhibit stable hydrophobicity (>150°) even after long-term aging, highlighting the durability of the designed system. Thermal cycling tests (10 cycles, 25°C–80°C) further confirm the structural and functional resilience of these foams under service-relevant conditions, with no pore collapse observed by SEM and negligible change in radial thermal conductivity (≤2.2%) across all cycles. Importantly, the study reveals a clear composition-dependent structure–property relationship, where moderate halloysite loading (≈5 wt%) provides the optimal balance between porosity, structural integrity, and multifunctional performance, while higher loadings lead to partial densification and reduced efficiency. Despite the introduction of inorganic components, the foams remain within the performance envelope of lightweight thermal insulators, confirming that the insulating regime is preserved without reaching a percolation threshold.

Compared to conventional nanocellulose aerogels, polymer foams, and silica aerogels, the present system uniquely bridges the gap between insulation performance and fire safety, achieving multifunctionality without relying on halogenated or phosphorus-based additives. This highlights the effectiveness of combining hierarchical structural design with sustainable material chemistry. Overall, this work establishes a scalable and environmentally benign strategy for designing next-generation porous materials with integrated functionalities. The NFC–AKD–HNT nanofoams represent a promising platform for advanced thermal insulation, fire-safe construction materials, and lightweight structural applications, and provide fundamental insights into the design of multifunctional bio-based aerogels governed by coupled structure–transport–property relationships.

4 | Experimental Section

4.1 | Materials

Nanofibrillated cellulose (NFC, 3 wt.% solid content) was obtained from the Process Development Center, University of Maine (USA). Halloysite nanoclay (HNT; diameter × length: 30–70 nm × 1–3 μm) and were purchased from Sigma--Aldrich (Germany). Alkyl ketene dimer (AKD) was supplied by Biosynth Ltd. (UK). Ultrapure water produced by a Milli-Q purification system (Millipore, USA) was used for all sample preparations.

4.2 | Preparation of Nanocellulose and Nanocomposite Foams

A 50 g of a 3 wt.% NFC was mixed with 50 mL of a 5 wt.% AKD solution and stirred mechanically at 300 rpm for 15 min under ambient conditions. Subsequently, HNT nanoclay was incorporated at concentrations of 1, 5, or 10 wt.% (relative to the total solid content), and stirring was continued until a visually homogeneous dispersion was obtained. After a total stirring time of 1 h, the resulting dispersions were cast into molds (24-well polystyrene plates, 10 mL polystyrene Falcon tubes and 8 cm circular aluminum disc) and freeze-dried for 48 h at a pressure of approximately 10^{-3} mbar and a temperature of −25°C. Control samples were prepared under identical conditions, except that AKD and HNT were omitted. The freeze-dried samples were designated NFC (neat nanocellulose), NAH_x (x = 1, 5, 10; denoting the HNT content in wt.%).

4.3 | Attenuated Total Reflection Fourier Transform Infrared Spectroscopy

The chemical structure/composition of the polymers were analyzed using a Bruker Alpha attenuated total reflection Fourier transform infrared (ATR–FTIR) spectrometer at a scan range of 4000–650 cm^{-1}. A total of 32 scans were performed with a resolution of 4 cm^{-1}.

4.4 | Powder X-Ray Diffraction (XRD)

The powder X-ray diffraction of all samples was investigated with an X-ray diffractometer (XRD, Bruker D8 Advance equipped with Cu Kα radiation). The scaffolds were cut into small pieces and deposited on the sample holder, and the XRD patterns were recorded at room temperature between a scattering angle (2θ) 4° to 70° and steps of 0.02°, and a scan rate of 0.02° 2θ s^{-1}.

4.5 | Density Analysis

The bulk density (ρ) of each foam sample was determined from its mass and geometric volume according to:

$$\rho = \frac{m}{v} \tag{3}$$

where m represents mass of sample in gram, and v, volume in cm^3. For each sample 3 repetition were made and average density was calculated.

Sample density was measured using a 50 mL pycnometer at 23°C (where density (ρ) of water = 0.9973 g·mL^{-1}). The procedure involved: (1) weighing the water-filled pycnometer (mL, m_1), (2) weighing the dry pycnometer with sample (m_s), and (3) weighing the pycnometer filled with water after sample removal (m_2). Sample density was calculated as:

$$\rho_s = \rho_{H_2O} \frac{m_s}{m_s + m_1 - m_2} \tag{4}$$

16136829, 0, Downloaded from https://onlinelibrary.wiley.com/doi/10.1002/smll.75920 by Dtsch Zentrum F. Luft-U. Raum Fahrt In D. Helmholtz Gemein., Wiley Online Library on [27/09/2026]. See the Terms and Conditions (https://onlinelibrary.wiley.com/terms-and-conditions) on Wiley Online Library for rules of use; OA articles are governed by the applicable Creative Commons License

4.6 | Scanning Electron Microscopy and Electron-Dispersive X-Ray Spectroscopy (SEM-EDX)

Samples were characterized by scanning electron microscope (SEM) using Zeiss Ultra 55, Carl Zeiss Microscope, operating with secondary electron (SE) mode. Energy-dispersive X-ray spectroscopy (EDX) for electron mapping analyses was carried out using Oxford Instruments Ultim Max 100 (Software AZtec 4.2). Baltec sputter coater apparatus was employed for the sputter coating of the samples with platinum element.

4.7 | µ-Tomographic Analyses

X-ray µ-CT analysis was performed in the Nanotom 160NF (Phoenix |X-ray) with three different samples, namely NFC (~5 × 6 × 2 mm^3), NAH1 (~2 × 2 × 5 mm^3) and NAH10 (~2 × 2 × 5 mm^3). Four images were collected per degree of rotation. The X-ray source was operated with 50 kV and 190 µA (for NFC) and 80 kV and 180 µA (for NAH and NAH10). The reconstruction of the images was performed with datos| x2-reconstruction software (GE Sensing & Inspection Technologies GmbH). In each case a volume of 1 × 1 × 1 mm^3 was reconstructed, which contained 250 × 250 × 250 voxel (edge length of voxel: 4 µm) and 500 × 500 × 500 voxel for NAH1 as well as NAH10 (edge length of voxel: 2 µm). The visualization and analysis of the reconstructed volume was performed with AVIZO 2019.3 software (Thermo Fisher Scientific).

4.8 | BET Isotherm

A Micromeritics TriStar II Surface Area and Porosity Analyzer was used to measure the isotherms of nitrogen adsorption and desorption at the temperature of liquid nitrogen. The TriStar II 3020 version 3.02 software was used to analyze the data. The samples were degassed overnight at 120°C in a vacuum to remove all adsorbed impurities before the measurements began. The specific surface area was determined with the Brunauer–Emmett–Teller (BET) method using nitrogen adsorption measurements within the relative pressure (P/P_0) range of 0.04–0.2 using a three-point analysis. This approach is particularly suitable for porous materials where low-pressure data minimizes the interference between multiple adsorption layers and ensures an accurate estimate of the monolayer capacity.

4.9 | Water Contact Angle Measurements

The surface wettability of all freeze-dried samples was investigated through Static Water Contact Angle SCA(H_2O) measurements using an OCA 35 Optical Contact Angle Meter and SCA 20 (version 4.1.12) software (DataPhysics Instruments, Filderstadt, Germany). Each SCA(H_2O) value was determined within 2 s of contact with the surface and is the average of at least six liquid droplets per surface. Two independent surfaces were used for each sample. Measurements were performed in triplicates at 25°C, using a 3 µL drop of ultrapure water (Milli-Q, resistivity of 18.2 MΩ cm at 25°C). For long-term stability assessment, the NFC and NFC–AKD–HNT foams were stored in falcon tubes (50 mL) for more than six years under standard laboratory ambient conditions (20°C–25°C, 40%–60% relative humidity) on open shelves without sealing or special protection from light. Contact angle measurements after storage revealed values within the experimental error of the initial measurements, indicating robust hydrophobicity under non-ideal, open-environment conditions

4.10 | Mechanical Properties

A uniaxial compression mechanical test was performed on a 1 kN universal testing machine, INSTRON (Model 5543, single head machine with Bluehill2 Software), using a cube-shaped samples (dimension ca.: 11 × 11 × 11 mm). For all the samples, a force head with a 500 N load cell was employed. The compression rate was 1 mm/min and the experiments were performed via traverse control. The load was measured and the traverse-load curve was determined. The slope of the curve in elastic region was used to calculate the modulus under uniaxial, vertical compressive loading. The mechanical data presented below are average values of the three measurements.

4.11 | Thermal Analysis

4.11.1 | Thermogravimetric Analysis (TGA)

TGA was performed on a TGA 4000 thermal analyzer from Perkin Elmer (Waltham, Massachusetts, USA) instrument in a nitrogen atmosphere (20 mL min^{-1}) of 40°C to 900°C at a heating rate of 10°C min^{-1} using an Al_2O_3 crucible without a lid. The Pyris software, Version 10.02.0468, was used for data evaluation.

4.11.2 | Thermal Conductivity

The thermal conductivity measurements were carried out using the HOT DISK TPS 2500 S (Hot Disk, Gothenburg, Sweden). The thermal conductivity of the hot disk is a transient measurement system in accordance with ISO 22007-2. Software, Hot Disk Thermal Constants Analyzer 7.3 was used for the measurements. Kapton-insulated sensor with design 5501 having a radius of 6.4 mm was used for the sample analyses. The set measurement parameter for the sensor was 0.02 W at 20 s and the sample temperature was about 20°C. A total of three measurements was carried out in order to make a statistical data. 4.12 Thermal cycling test.

Thermal cycling stability of the nanocomposite foams was assessed using a [TR5-100] thermal cycling chamber (LIB Environmental Simulation Industry, Xi'an, China). Foam cylinder samples of NFC, NAH1, and NAH10 were subjected to 10 programmed thermal cycles between room temperature (25°C) and 80°C at a ramp rate of 10°C min^{-1}, with a controlled dwell time of 1 h at each temperature setpoint. Macroscopic dimensions (height and diameter) were recorded before and after cycling using digital calipers. For NAH10, radial thermal conductivity was measured after each set of cycles (cycles 1–3, 4–6, and 7–10) using the HOT DISK TPS 2500 S instrument (ISO 22007-2) under identical conditions to those described above, with samples fully equilibrated to room temperature (~25°C)

16136829, 0, Downloaded from https://onlinelibrary.wiley.com/doi/10.1002/smll.75920 by Dtsch Zentrum F. Luft-U. Raum Fahrt In D. Helmholtz Gemein., Wiley Online Library on [27/09/2026]. See the Terms and Conditions (https://onlinelibrary.wiley.com/terms-and-conditions) on Wiley Online Library for rules of use; OA articles are governed by the applicable Creative Commons License

prior to each measurement. SEM imaging of cross-sections of the same NAH10 sample was performed at room temperature before the first thermal cycle (25°C, baseline) and after cooling to room temperature following the final 80°C dwell of cycle 10, as described in Section 4.6, to assess preservation of the pore architecture after the complete cycling program.

4.11.3 | Flame Retardance Test

Vertical burning test and horizontal burning test have been conducted for freeze-dried aerogels (length x diameter: 1.3 cm × 6 cm) in an in-house setup facility according to UL 94. For the vertical burning test, the flame height was kept as 2 cm and flame propagation time was 10 s for consecutive 6 times. The horizontal burning test has been conducted according to method of UL 94 HBF, specifically designed for foamed material. During analysis, the flame height was kept as 38 mm and propagated for more than 60 s. The burned part of nanocomposite foam was measured and average of 3 repetition was calculated.

4.11.4 | Insulation

For the insulation test a heating plate MR2002 (Heidolph, Schwabach, Germany) and a long wavelength infrared camera (LWIR) PI450 (Optris, Berlin, Germany) were used. The heating plate was set to 130°C and the sample cylinders (height 20.07 ± 0.48 mm, diameter 13.61 ± 0.61 mm) were placed on the hot plate, with a distance of 200 mm to the LWIR camera. The heat evolvement in the cylinder was monitored for 15 min, and the temperature on top of the sample was measured instantly after the sample was placed on the plate and after 15 min.

Author Contributions

Tamilselvan Mohan: writing – original draft, investigation, conceptualization, methodology, visualization, validation, writing – review editing, supervision, data curation. **Doris Bračič**: data curation validation, visualization, writing – review editing, investigation, methodology. **Chandran Nagaraj**: methodology validation, visualization, writing – review editing, data curation. **Thomas Harter**: methodology, validation, visualization, writing – review editing, formal analysis, data curation, resources. **Resul Fener**: methodology, validation, visualization, writing – review editing, formal analysis, data curation, resources. **Anne Dennstedt**: visualization, validation, methodology, writing – review editing, formal analysis, data curation, resources. **Barbara Milow**: resources, data curation formal analysis, visualization, validation, methodology, writing – review editing, investigation. **KathirvelGanesan**: writing – original draft, writing – review editing, formal analysis, software, data curation, supervision, validation, methodology, visualization, investigation. **Ulrich Hirn**: methodology, validation visualization, writing – review editing, formal analysis, data curation, resources. **Rupert Kargl**: validation, methodology, writing – review editing, visualization, supervision, data curation. **Karin Stana Kleinscheck**: investigation, funding acquisition, writing – review editing, supervision, resources, conceptualization.

Acknowledgements

The work was carried out within the RDI project Cel.Cycle: Potential of biomass for development of advanced materials and bio-based products« (Contract No. OP20.00365), and the financial support from the Slovenian Research Agency for Research (Grant No. P2-0118). CN was supported by the Austrian Science Foundation (FWF, Grant DOI 10.55776/PAT7985824). The authors used Perplexity.AI (USA) to assist with language, readability, and scientific data search.

Open Access funding provided by Technische Universitat Graz.

Conflicts of Interest

The authors declare no conflicts of interest.

Data Availability Statement

The data that support the findings of this study are available from the corresponding author upon reasonable request.

References

1. M. F. Ashby, "Chapter 6 – Case Studies: Materials Selection," in *Materials Selection in Mechanical Design*, 4th ed, ed. M. F. Ashby, (Butterworth-Heinemann, 2011), 125–195, https://doi.org/10.1016/B978-1-85617-663-7.00006-0.

2. A. Bahadori, "Chapter Three—Material Selection for Thermal Insulation," in *Thermal Insulation Handbook for the Oil, Gas, and Petrochemical Industries*, ed. A. Bahadori, (Gulf Professional Publishing, 2014), 239–301, https://doi.org/10.1016/B978-0-12-800010-6.00003-4.

3. A. Dasari, Z. Z. Yu, G. P. Cai, and Y. W. Mai, "Recent Developments In The Fire Retardancy Of Polymeric Materials," *Progress in Polymer Science* 38, no. 9 (2013): 1357–1387, https://doi.org/10.1016/j.progpolymsci.2013.06.006.

4. X. Chen, Z. Zhang, C. Hu, Y. Zhao, S. Wang, and C. Huang, "Thermal Insulation Nanofiber Aerogels: A Journey From Structure Construction to Multifunctionalization," *Small* 21, no. 31 (2025): 2502291, https://doi.org/10.1002/smll.202502291.

5. B. Wicklein, A. Kocjan, G. Salazar-Alvarez, et al., "Thermally Insulating And Fire-Retardant Lightweight Anisotropic Foams Based On Nanocellulose And Graphene Oxide," *Nature Nanotechnology* 10, no. 3 (2015): 277–283, https://doi.org/10.1038/nnano.2014.248.

6. Z. Fu, J. Corker, T. Papathanasiou, et al., "Critical Review On The Thermal Conductivity Modelling Of Silica Aerogel Composites," *Journal of Building Engineering* 57 (2022): 104814, https://doi.org/10.1016/j.jobe.2022.104814.

7. H. Sun, D. Zheng, Y. Zhu, et al., "Multiscale Design for Robust, Thermal Insulating, and Flame Self-Extinguishing Cellulose Foam," *Small* 20, no. 12 (2024): 2306942, https://doi.org/10.1002/smll.202306942.

8. X. Wang, C. Yao, F. Wang, and Z. Li, "Cellulose-Based Nanomaterials for Energy Applications," *Small* 14, no. 10 (2018): 1704152, https://doi.org/10.1002/smll.201704152.

9. L. Wang, X. Lin, F. Liu, et al., "Flame-Retardant Aerogels And Porous Composites Based On Sustainable Biomass Polysaccharides: A Review," *Journal of Building Engineering* 112 (2025): 113806, https://doi.org/10.1016/j.jobe.2025.113806.

10. U. Jančič, M. Bračič, A. Ojstršek, M. Božič, T. Mohan, and S. Gorgieva, "Consolidation of Cellulose Nanofibrils With Lignosulphonate Bio-Waste Into Excellent Flame Retardant and UV Blocking Membranes," *Carbohydrate Polymers* 251: 117126, https://doi.org/10.1016/j.carbpol.2020.117126.

11. C. D. Simão, J. S. Reparaz, M. R. Wagner, et al., "Optical and Mechanical Properties Of Nanofibrillated Cellulose: Toward A Robust Platform For Next-Generation Green Technologies," *Carbohydrate Polymers* 126 (2015): 40–46, https://doi.org/10.1016/j.carbpol.2015.03.032.

12. A. S. González-Ugarte, I. Hafez, and M. Tajvidi, "Characterization and Properties Of Hybrid Foams From Nanocellulose And Kaolin-Microfibrillated Cellulose Composite," *Scientific Reports* 10, no. 1 (2020): 17459, https://doi.org/10.1038/s41598-020-73899-z.

13. Y. Chen, L. Zhang, Y. Yang, et al., "Recent Progress on Nanocellulose Aerogels: Preparation, Modification, Composite Fabrication, Applica-

16136829, 0, Downloaded from https://onlinelibrary.wiley.com/doi/10.1002/smll.75920 by Dtsch Zentrum F. Luft-U. Raum Fahrt In D. Helmholtz Gemein., Wiley Online Library on [27/09/2026]. See the Terms and Conditions (https://onlinelibrary.wiley.com/terms-and-conditions) on Wiley Online Library for rules of use; OA articles are governed by the applicable Creative Commons License

tions," *Advanced Materials* 33, no. 11: 2005569, https://doi.org/10.1002/adma.202005569.

14. N. Lavoine and L. Bergström, "Nanocellulose-based Foams And Aerogels: Processing, Properties, And Applications," *Journal of Materials Chemistry A* 5, no. 31 (2017): 16105–16117, https://doi.org/10.1039/C7TA02807E.

15. V. Apostolopoulou-Kalkavoura, P. Munier, and L. Bergström, "Thermally Insulating Nanocellulose-Based Materials," *Advanced Materials* 33, no. 28: 2001839, https://doi.org/10.1002/adma.202001839.

16. T. A. Nguyen, T. B. Nguyen, D. Q. Tran, et al., "Bio-Functional Nanocellulose/Lignocellulose-Based Polyurethane Nanocomposite Foams With Enhanced Flame Retardancy, Thermal Conductivity, And Thermal Stability," *International Journal of Biological Macromolecules* 305 (2025): 141133, https://doi.org/10.1016/j.ijbiomac.2025.141133.

17. K. Stana-Kleinschek, H. M. A. Ehmann, and S. Spirk, "Cellulose and Other Polysaccharides Surface Properties and Their Characterisation," in *The European Polysaccharide Network of Excellence (EPNOE): Research Initiatives and Results*, ed. P. Navard (Springer, 2012), 215–251.

18. H. Sehaqui, A. Liu, Q. Zhou, and L. A. Berglund, "Fast Preparation Procedure for Large, Flat Cellulose and Cellulose/Inorganic Nanopaper Structures," *Biomacromolecules* 11 (2010): 2195–2198.

19. T. Fan, Z. Yan, W. Huang, et al., "A Comprehensive Review Of Contents, Toxic Effects, Metabolisms, And Environmental Behaviors Of Brominated And Organophosphorus Flame Retardants," *Journal of Hazardous Materials* 496 (2025): 139428, https://doi.org/10.1016/j.jhazmat.2025.139428.

20. P. Kiliaris and C. D. Papaspyrides, "Polymer/Layered Silicate (Clay) Nanocomposites: An Overview of Flame Retardancy," *Progress in Polymer Science* 35, no. 7 (2010): 902–958, https://doi.org/10.1016/j.progpolymsci.2010.03.001.

21. J. T. Korhonen, M. Kettunen, R. H. A. Ras, and O. Ikkala, "Hydrophobic Nanocellulose Aerogels as Floating, Sustainable, Reusable, and Recyclable Oil Absorbents," *ACS Applied Materials & Interfaces* 3, no. 6 (2011): 1813–1816, https://doi.org/10.1021/am200475b.

22. T. Mohan, R. Kargl, A. Doliška, et al., "Wettability and Surface Composition Of Partly And Fully Regenerated Cellulose Thin Films From Trimethylsilyl cellulose," *Journal of Colloid and Interface Science* 358, no. 2 (2011): 604–610, https://doi.org/10.1016/j.jcis.2011.03.022.

23. P. Thomas, T. Duolikun, N. P. Rumjit, et al., "Comprehensive Review On Nanocellulose: Recent Developments, Challenges And Future Prospects," *Journal of the Mechanical Behavior of Biomedical Materials* 110 (2020): 103884, https://doi.org/10.1016/j.jmbbm.2020.103884.

24. B. E. Yoldas, M. J. Annen, and J. Bostaph, "Chemical Engineering of Aerogel Morphology Formed Under Nonsupercritical Conditions for Thermal Insulation," *Chemistry of Materials* 12, no. 8 (2000): 2475–2484, https://doi.org/10.1021/cm9903428.

25. M. Liu, Z. Jia, D. Jia, and C. Zhou, "Recent Advance In Research On Halloysite Nanotubes-Polymer Nanocomposite," *Progress in Polymer Science* 39, no. 8 (2014): 1498–1525, https://doi.org/10.1016/j.progpolymsci.2014.04.004.

26. M. Du, B. Guo, and D. Jia, "Thermal stability and flame retardant effects of halloysite nanotubes on poly(propylene)," *European Polymer Journal* 42, no. 6 (2006): 1362–1369, https://doi.org/10.1016/j.eurpolymj.2005.12.006.

27. H. Vahabi, R. Sonnier, A. Taguet, B. Otazaghine, M. R. Saeb, and G. Beyer, "3 – Halloysite nanotubes (HNTs)/polymer nanocomposites: Thermal degradation and flame retardancy," in *Clay Nanoparticles*, eds. G. Cavallaro, R. Fakhrullin, and P. Pasbakhsh, (Elsevier, 2020), 67–93.

28. G. Cavallaro, S. Milioto, and G. Lazzara, "Halloysite Nanotubes: Interfacial Properties and Applications in Cultural Heritage," *Langmuir* 36, no. 14 (2020): 3677–3689, https://doi.org/10.1021/acs.langmuir.0c00573.

29. B. Lecouvet, M. Sclavons, S. Bourbigot, and C. Bailly, "Thermal and Flammability Properties Of Polyethersulfone/Halloysite Nanocomposites Prepared By Melt Compounding," *Polymer Degradation and Stability* 98, no. 10 (2013): 1993–2004, https://doi.org/10.1016/j.polymdegradstab.2013.07.013.

30. A. Karademir, D. Hoyland, N. Wiseman, and H. Xiao, "A Study Of The Effects Of Alkyl Ketene Dimer And Ketone On Paper Sizing And Friction Properties," *Appita Journal* 57, no. 2 (2004): 116–120.

31. M. Bračič, J. Malešič, M. Brunčko, et al., "Functional Coatings With Ethyl Cellulose-Calcium Carbonate Alkaline Nanoparticles For Deacidification And Mechanical Reinforcement Of Paper Artifacts," *Surfaces and Interfaces* 60 (2025): 106065, https://doi.org/10.1016/j.surfin.2025.106065.

32. A. Dobaj Štiglic, F. Lackner, C. Nagaraj, et al., "3D-Printed Collagen–Nanocellulose Hybrid Bioscaffolds With Tailored Properties for Tissue Engineering Applications," *ACS Applied Bio Materials* 6, no. 12 (2023): 5596–5608, https://doi.org/10.1021/acsabm.3c00767.

33. A. D. Štiglic, F. Gürer, F. Lackner, et al., "Organic Acid Cross-Linked 3D Printed Cellulose Nanocomposite Bioscaffolds With Controlled Porosity, Mechanical Strength, And Biocompatibility," *Iscience* 25, no. 5 (2022): 104263, https://doi.org/10.1016/j.isci.2022.104263.

34. T. Mohan, A. Dobaj Štiglic, M. Beaumont, et al., "Generic Method for Designing Self-Standing and Dual Porous 3D Bioscaffolds From Cellulosic Nanomaterials for Tissue Engineering Applications," *ACS Applied Bio Materials* 3, no. 2 (2020): 1197–1209, https://doi.org/10.1021/acsabm.9b01099.

35. S. Hosseini, R. Nilsson, A. Ström, A. Larsson, and G. Westman, "Alkyl Ketene Dimer Modification Of Thermomechanical Pulp Promotes Processability With Polypropylene," *Polymer Composites* 45, no. 1 (2024): 825–835, https://doi.org/10.1002/pc.27818.

36. Y. Yan, H. Amer, T. Rosenau, et al., "Dry, Hydrophobic Microfibrillated Cellulose Powder Obtained In A Simple Procedure Using Alkyl Ketene Dimer," *Cellulose* 23, no. 2 (2016): 1189–1197, https://doi.org/10.1007/s10570-016-0887-0.

37. T. Lovaglio, W. Gindl-Altmutter, T. Meints, N. Moretti, and L. Todaro, "Wetting Behavior of Alder (Alnus cordata (Loisel) Duby) Wood Surface: Effect of Thermo-Treatment and Alkyl Ketene Dimer (AKD)," *Forests* 10, no. 9 (2019): 770, https://doi.org/10.3390/f10090770.

38. J. Yu, S. Boudjelida, F. Galiano, A. Figoli, M. Bonchio, and M. Carraro, "Porous Polymeric Membranes Doped With Halloysite Nanotubes and Oxygenic Polyoxometalates," *Advanced Materials Interfaces* 9, no. 11 (2022): 2102152, https://doi.org/10.1002/admi.202102152.

39. P. Yuan, D. Tan, F. Annabi-Bergaya, et al., "Changes in Structure, Morphology, Porosity, and Surface Activity of Mesoporous Halloysite Nanotubes Under Heating," *Clays and Clay Minerals* 60, no. 6 (2012): 561–573, https://doi.org/10.1346/CCMN.2012.0600602.

40. H. Chu, Z. Chen, Y. Chen, D. Wei, Y. Liu, and H. Zhao, "Mechanical Properties and Crystallinity of Specific PLA/Cellulose Composites by Surface Modification of Nanofibrillated Cellulose," *Polymers* 16, no. 17 (2024): 2474, https://doi.org/10.3390/polym16172474.

41. X. Yang, Y. Zhang, D. Zheng, J. Yue, and M. Liu, "Nano-Biocomposite Films Fabricated From Cellulose Fibers And Halloysite Nanotubes," *Applied Clay Science* 190 (2020): 105565, https://doi.org/10.1016/j.clay.2020.105565.

42. N. A. Hanid, M. U. Wahit, Q. Guo, S. Mahmoodian, and M. Soheilmoghaddam, "Development of Regenerated Cellulose/Halloysites Nanocomposites via Ionic Liquids," *Carbohydrate Polymers* 99 (2014): 91–97, https://doi.org/10.1016/j.carbpol.2013.07.080.

43. H. Li, J. Yang, X. Feng, and Z. Qin, "Cellulose Nanofiber-Assisted Dispersion of Halloysite Nanotubes via Silane Coupling Agent-Reinforced Starch–PVA Biodegradable Composite Membrane," *Membranes* 12, no. 2 (2022): 169, https://doi.org/10.3390/membranes12020169.

44. H. Sehaqui, Q. Zhou, and L. A. Berglund, "High-Porosity Aerogels Of High Specific Surface Area Prepared From Nanofibrillated Cellulose (NFC)," *Composites Science and Technology* 71, no. 13 (2011): 1593–1599, https://doi.org/10.1016/j.compscitech.2011.07.003.

16136829, 0, Downloaded from https://onlinelibrary.wiley.com/doi/10.1002/smll.75920 by Dtsch Zentrum F. Luft-U. Raum Fahrt In D. Helmholtz Gemein., Wiley Online Library on [27/09/2026]. See the Terms and Conditions (https://onlinelibrary.wiley.com/terms-and-conditions) on Wiley Online Library for rules of use; OA articles are governed by the applicable Creative Commons License

45. M. Wang, H. Cao, Z. Huang, et al., "Robust Cellulose/Clay Composite Aerogels With Frame-Wall Like Structure For Superior Thermal Insulation And Flame Retardancy," *Composites Part B: Engineering* 309 (2026): 113098, https://doi.org/10.1016/j.compositesb.2025.113098.

46. K. J. De France, T. Hoare, and E. D. Cranston, "Review of Hydrogels and Aerogels Containing Nanocellulose," *Chemistry of Materials* 29, no. 11 (2017): 4609–4631, https://doi.org/10.1021/acs.chemmater.7b00531.

47. M. S. El-Feky, A. H. Badawy, P. Youssef, and M. Kohail, "Utilizing Industrial Byproducts For The Manufacture Of Clay-Cellulose Nanocomposite Cements With Enhanced Sustainability," *Scientific Reports* 14, no. 1 (2024): 751, https://doi.org/10.1038/s41598-023-51130-z.

48. M. N. Uddin, P. S. Dhanasekaran, and R. Asmatulu, "Mechanical Properties Of Highly Porous PEEK Bionanocomposites Incorporated With Carbon And Hydroxyapatite Nanoparticles For Scaffold Applications," *Progress in Biomaterials* 8, no. 3 (2019): 211–221, https://doi.org/10.1007/s40204-019-00123-1.

49. L. J. Gibson, "Biomechanics of Cellular Solids," *Journal of Biomechanics* 38, no. 3 (2005): 377–399, https://doi.org/10.1016/j.jbiomech.2004.09.027.

50. M. F. Ashby, "The Properties Of Foams And Lattices," *Philosophical Transactions of the Royal Society A: Mathematical, Physical and Engineering Sciences* 364 (1838): 15–30, https://doi.org/10.1098/rsta.2005.1678.

51. H. Gao, M. A. Soto, Z. Li, L. J. Andrew, and M. J. MacLachlan, "Cellulose Nanocrystal/Halloysite Nanotube Composite Aerogels For Water Purification," *Dalton Transactions* 52, no. 36 (2023): 12968–12977, https://doi.org/10.1039/D3DT01908J.

52. M. Long, X. Yang, T. Shi, and Y. Yang, "All-Natural Aerogel Of Nanoclay/Cellulose Nanofibers With Hierarchical Porous Structure For Rapid Hemostasis," *International Journal of Biological Macromolecules* 278 (2024): 134592, https://doi.org/10.1016/j.ijbiomac.2024.134592.

53. X. Ma, C. Yang, X. Feng, H. Shang, Y. Zhao, and B. Zhang, "Halloysite-Based Aerogels For Efficient Encapsulation Of Phase Change Materials With Excellent Solar Energy Storage And Retrieval Performance," *Applied Energy* 341 (2023): 121101, https://doi.org/10.1016/j.apenergy.2023.121101.

54. D. K. Shen and S. Gu, "The Mechanism For Thermal Decomposition Of Cellulose And Its Main Products," *Bioresource Technology* 100, no. 24 (2009): 6496–6504, https://doi.org/10.1016/j.biortech.2009.06.095.

55. Y. Yu, Z. Zhuang, W. Zhang, T. Xue, C. Wang, and Y. Yin, "Cellulose-Based Aerogel Fibers With Enhanced Mechanical Properties For Thermal Insulation And Humidity Response," *International Journal of Biological Macromolecules* 323 (2025): 147053, https://doi.org/10.1016/j.ijbiomac.2025.147053.

56. M. Farooq, M. H. Sipponen, A. Seppälä, and M. Österberg, "Eco-friendly Flame-Retardant Cellulose Nanofibril Aerogels by Incorporating Sodium Bicarbonate," *ACS Applied Materials & Interfaces* 10, no. 32 (2018): 27407–27415, https://doi.org/10.1021/acsami.8b04376.

57. A. Lo Bianco, M. M. Calvino, G. Lazzara, S. Milioto, and G. Cavallaro, "Geopolymerization of Halloysite Clay Nanotubes Mixed With Hydroxypropyl Cellulose For Development Of Composite Films With Flame Resistance Properties," *Ceramics International* 52 (2025): 15130–15138, https://doi.org/10.1016/j.ceramint.2025.06.260.

58. M. A. Shahat and W. Soliman, "Lightweight Thermally Insulating Fired Clay Bricks Enhanced With Chitosan-Based Clay Nanocomposites For Sustainable Construction," *Scientific Reports* 15, no. 1 (2025): 26528, https://doi.org/10.1038/s41598-025-11790-5.

59. Y. Yang, Y. Chen, Y. Li, et al., "Interfacial Assembly Of Nanocellulose Microgels Enhances Thermal Insulation Of Pickering Foam," *International Journal of Biological Macromolecules* 282 (2024): 136796, https://doi.org/10.1016/j.ijbiomac.2024.136796.

60. L. Wang, Y. Tian, Y. Chang, L. Chen, and Q. Zhang, "Cellulose Nanofiber-Created Air Barrier Enabling Closed-Cell Foams Prepared via Oven-Drying," *Carbohydrate Polymers* 351 (2025): 123096, https://doi.org/10.1016/j.carbpol.2024.123096.

61. J. H. Qiao, R. Bolot, H. L. Liao, and C. Coddet, "Knudsen Effect on the Estimation of the Effective Thermal Conductivity of Thermal Barrier Coatings," *Journal of Thermal Spray Technology* 22, no. 2 (2013): 175–182, https://doi.org/10.1007/s11666-012-9878-3.

62. B. Notario, J. Pinto, E. Solorzano, J. A. de Saja, M. Dumon, and M. A. Rodríguez-Pérez, "Experimental validation of the Knudsen effect in nanocellular polymeric foams," *Polymer* 56 (2015): 57–67, https://doi.org/10.1016/j.polymer.2014.10.006.

63. A. L. Missio, C. G. Otoni, B. Zhao, et al., "Nanocellulose Removes the Need for Chemical Crosslinking in Tannin-Based Rigid Foams and Enhances Their Strength and Fire Retardancy," *ACS Sustainable Chemistry & Engineering* 10, no. 31 (2022): 10303–10310, https://doi.org/10.1021/acssuschemeng.2c02678.

64. Y. X. Chen, S. Sepahvand, F. Gauvin, K. Schollbach, H. J. H. Brouwers, and Q. Yu, "One-Pot Synthesis Of Monolithic Silica-Cellulose Aerogel Applying A Sustainable Sodium Silicate Precursor," *Construction and Building Materials* 293 (2021): 123289, https://doi.org/10.1016/j.conbuildmat.2021.123289.

65. H. Zhang, W. Z. Fang, Y. M. Li, and W. Q. Tao, "Experimental Study Of The Thermal Conductivity Of Polyurethane Foams," *Applied Thermal Engineering* 115 (2017): 528–538, https://doi.org/10.1016/j.applthermaleng.2016.12.057.

66. A. Simpson, I. Rattigan, E. Kalavsky, and G. Parr, "Thermal Conductivity And Conditioning Of Grey Expanded Polystyrene Foams," *Cellular Polymers* 39, no. 6 (2020): 238–262, https://doi.org/10.1177/0262489320934263.

Supporting Information

Additional supporting information can be found online in the Supporting Information section.

Supporting File: smll75920-sup-0001-SuppMat.docx.

16136829, 0, Downloaded from https://onlinelibrary.wiley.com/doi/10.1002/smll.75920 by Dtsch Zentrum F. Luft-U. Raum Fahrt In D. Helmholtz Gemein., Wiley Online Library on [27/09/2026]. See the Terms and Conditions (https://onlinelibrary.wiley.com/terms-and-conditions) on Wiley Online Library for rules of use; OA articles are governed by the applicable Creative Commons License